CLICdp-Note-2014-003
21 August 2014

Physics potential of the $\sigma_{e^+e^-\to H\nu_e\bar{\nu}_e} \times BR_{H\to Z\gamma}$ measurement at a 1.4 TeV Compact Linear Collider

C. Grefe*, E. Sicking[1)]*

On behalf of the CLICdp collaboration

* *CERN, Switzerland*

Abstract

We present a benchmark study of the cross section times branching ratio measurement for the process $e^+e^- \to H\nu_e\bar{\nu}_e; H \to Z\gamma$ evaluated at a 1.4 TeV e^+e^- Compact Linear Collider (CLIC) using the CLIC_SiD_CDR detector model. The study is based on a full GEANT4 detector simulation and reconstruction of signal and background processes, including $\gamma\gamma \to$ hadrons background events. The combined statistical precision of $\sigma_{e^+e^-\to H\nu_e\bar{\nu}_e} \times BR_{H\to Z\gamma}$, including the Z decay channels $Z \to q\bar{q}$, $Z \to e^+e^-$, and $Z \to \mu^+\mu^-$, for an integrated luminosity of 1.5 ab^{-1}, is estimated to be approximately 42%. For a CLIC collider with -80% (left-handed) electron beam polarisation, the uncertainty can be reduced to approximately 31%.

This work was carried out in the framework of the CLICdp collaboration

[1] eva.sicking@cern.ch

Contents

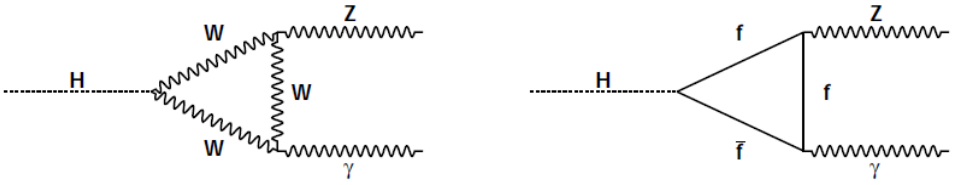

Figure 1: Leading order Feynman diagrams for the Standard Model Higgs decay $H \to Z\gamma$.

1. Introduction

In the Standard Model of particle physics (SM), the Higgs boson decay $H \to Z\gamma$ is induced at leading order by loops over heavy charged particles, such as the W boson, or heavy fermions, such as the top quark. The leading order Feynman diagrams are shown in Figure 1. In addition to the particles of the SM, particles of theories beyond the SM (BSM) could contribute in these loops. Deviations from the SM expectation of the branching ratio $BR_{H\to Z\gamma}$ could therefore give an insight into BSM processes. Furthermore, a study of this process allows for an estimation of the capability to study very rare processes.
While the Higgs boson has been discovered and studied at the LHC in other decay modes [1, 2], up to now no evidence for the rare $H \to Z\gamma$ decay has been found [3, 4].
In the following, a benchmark study of the cross section times branching ratio measurement of the process $e^+e^- \to H\nu_e\bar{\nu}_e; H \to Z\gamma$ is presented. The study is performed at a e^+e^- Compact Linear Collider (CLIC) [5] with a centre-of-mass energy of $\sqrt{s} = 1.4\,\text{TeV}$, using the CLIC_SiD_CDR detector concept [6, 7] as described in the CLIC Conceptual Design Report (CDR) [8, 9]. The study is based on a simulated dataset corresponding to an integrated luminosity of $1.5\,\text{ab}^{-1}$, which could be recorded at CLIC in approximately 4 years of data taking. The study is part of an ongoing effort to estimate the physics potential of CLIC at various centre-of-mass energy stages, including $\sqrt{s} = 350\,\text{GeV}$, $\sqrt{s} = 1.4\,\text{TeV}$, and $\sqrt{s} = 3\,\text{TeV}$ [10].
The note is structured in the following way: Section 2 describes the simulation of signal and background processes. In Section 3, the performance of the photon reconstruction is discussed. Section 4 introduces the analysis strategy and Section 5 describes the event selection. The analysis results are presented in Section 6. In Section 7, possible ways to improve the results are discussed and in Section 8 conclusions are drawn. In the Appendix A, all event properties used in the signal and background event classification are shown. Appendix B describes an alternative method to extract the analysis results and the limitations of this method in the presented analysis.

2. Event samples

The simulation of signal and background processes is based on the same procedure as already used in studies presented in the CLIC CDR [8, 9]. Signal and background processes are simulated with the WHIZARD1 event generator [11, 12] in which the CLIC luminosity spectrum at 1.4 TeV is used [13], with initial state radiation (ISR) and beam recoil taken into account. The fragmentation and hadronisation of final state partons, as well as final state radiation, is simulated using PYTHIA6 [14].
After the event generation, a full CLIC_SiD_CDR detector simulation and reconstruction is performed. The detector simulation is performed using SLIC [15] based on GEANT4 [16, 17]. Before digitisation of the detector signals, $\gamma\gamma \to$ hadrons pileup events are overlayed on top of the physics process. The digitisation and track reconstruction is performed using `org.lcsim` [18]. The particle flow reconstruction and particle identification is performed using the particle flow algorithm PANDORAPFA [19, 20].

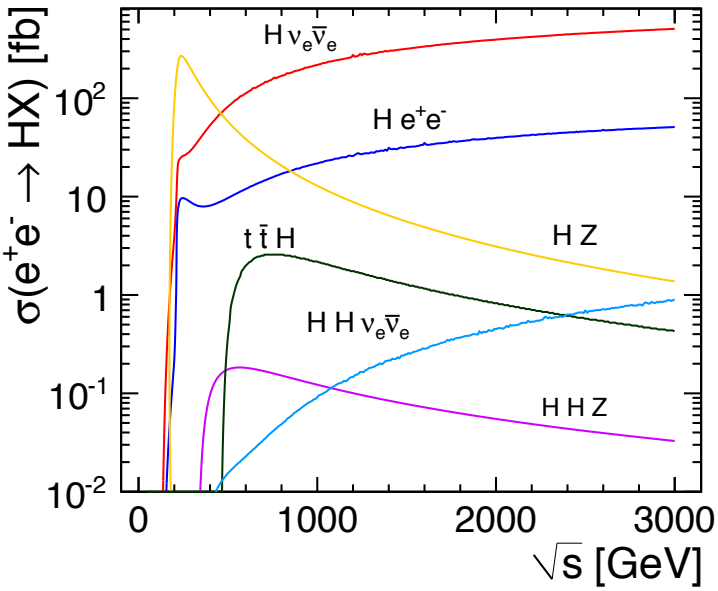

Figure 2: Cross section for SM Higgs production processes in e^+e^- collisions as a function of the centre-of-mass energy, taken from [10].

2.1. Signal

In e^+e^- collisions, at a centre-of-mass energy of $\sqrt{s} = 1.4\,\text{TeV}$ and for a SM Higgs mass of $M_H = 126\,\text{GeV}$ [1, 2], the dominant production process for the SM Higgs boson is W^+W^- fusion (cf. Figure 2). At this energy, and without beam polarisation, W^+W^- fusion has a cross section of $\sigma_{e^+e^-\to H\nu_e\bar{\nu}_e} = 244\,\text{fb}$ while all other Higgs production processes are more than 10 times less frequent. Therefore, only contributions from the dominant W^+W^- fusion production process are considered in the following.
The decay $H \to Z\gamma$ is expected to have a branching ratio of $BR_{H\to Z\gamma} = 0.16\%$ [21]. Hence the cross section times branching ratio $\sigma_{e^+e^-\to H\nu_e\bar{\nu}_e} \times BR_{H\to Z\gamma}$ has a value of 0.39 fb, resulting in 585 $H \to Z\gamma$ events expected for an integrated luminosity of $1.5\,\text{ab}^{-1}$.
Z bosons decay predominantly into a quark-antiquark or lepton-antilepton pairs. In this analysis, only the entirely visible Z decays are considered. These are those decays in which the Z either decays into a quark-antiquark pair ($BR_{Z\to q\bar{q}} \approx 70\%$, $q = u,d,s,c,b$) or into e^+e^- or $\mu^+\mu^-$ ($BR_{Z\to e^+e^-} \approx 3.6\%$, $BR_{Z\to\mu^+\mu^-} \approx 3.6\%$) [22]. Table 1 shows the number of expected events for $1.5\,\text{ab}^{-1}$ for the three signal channels, together with the number of simulated events used in this study. The three cases $Z \to q\bar{q}$, $Z \to e^+e^-$, and $Z \to \mu^+\mu^-$ are studied separately in the following.

2.2. Background

The visible final states of the signal channels $q\bar{q}\gamma$ or $l^+l^-\gamma$ (here $l = e,\mu$) are also produced in several background processes. In addition, photons can be produced as ISR, also allowing processes with $q\bar{q}$ or l^+l^- which originate, for example, from Z decays to contribute as background processes. Some of these background processes have much larger cross sections than the signal process, resulting in a large number of background events expected for $1.5\,\text{ab}^{-1}$.
In order to reduce the vast amount of background events which would have to be processed in the detector simulation, the following generator level cuts[2] are applied before the detector simulation of background

[2] Generator level cuts are also called STDHEP cuts.

Table 1: Cross section and expected and simulated number of signal events for an integrated luminosity of $1.5\,\mathrm{ab}^{-1}$ in the studied Higgs decay channels.

Process	$\sigma \times \mathrm{BR}_{\mathrm{H}\to\mathrm{Z}\gamma} \times \mathrm{BR}_{\mathrm{Z}}(\mathrm{fb})$	Expected events for $1.5\,\mathrm{ab}^{-1}$	Simulated events
$e^+e^- \to H\nu_e\bar{\nu}_e; H \to Z\gamma; Z \to q\bar{q}$	0.27	409	225855
$e^+e^- \to H\nu_e\bar{\nu}_e; H \to Z\gamma; Z \to e^+e^-$	0.014	21	170073
$e^+e^- \to H\nu_e\bar{\nu}_e; H \to Z\gamma; Z \to \mu^+\mu^-$	0.014	21	169748

events: the collision event should contain at least one photon and one $q\bar{q}$ or one l^+l^- pair, the reconstructed Higgs candidate should have an invariant mass of $100\,\mathrm{GeV} < M_{\mathrm{H}} < 150\,\mathrm{GeV}$, and each Higgs candidate daughter should have an energy of $E > 15\,\mathrm{GeV}$, a transverse momentum of $p_{\mathrm{T}} > 10\,\mathrm{GeV}$, and a polar angle between $10^\circ < \theta < 170^\circ$. In a later step of the analysis, pre-selection cuts are applied to all signal and background processes (cf. Section 5.1). These latter cuts are tighter than the generator level cuts and ensure that the generator level cuts will not bias the analysis results.

All background channels which are relevant for the $H \to Z\gamma$ study, after applying generator level cuts, are listed in Tables 2 and 3. Background channels from e^+e^- collisions are listed in Table 2, while those from $e^+\gamma$ and $e^-\gamma$ collisions are given in Table 3. In these processes, the initial state photon is either from beamstrahlung (BS) or from the equivalent photon approximation (EPA) [23]. The initial state $e^\pm\gamma$ from BS photons has a lower instantaneous luminosity than the initial state processes e^+e^- and $e^\pm\gamma$ from EPA [13]. Instead of $1.5\,\mathrm{ab}^{-1}$ in 4 years of data taking, only $1.125\,\mathrm{ab}^{-1}$ of $e^\pm\gamma$ collision events with photons from BS are expected. Processes with initial state $\gamma\gamma$ are found to be negligible for this study.

Some of the background processes relevant for this study have already been simulated for other studies of Higgs decays using the same experimental setup. These simulations have been performed without generator level cuts. These events are also included in the analysis. The corresponding background channels are marked in the tables with a dagger (†).

Table 2: Cross section and expected and simulated number of background events for an integrated luminosity of $1.5\,\mathrm{ab}^{-1}$ e^+e^- collisions which produce the same visible final state particles as the $H \to Z\gamma$ signal processes. All processes except those marked with a dagger (†) are simulated after applying generator level cuts. For all channels, additional final state photons are produced as ISR.

	Without cuts				With generator level cuts		
Process (- ISR)	σ(fb)	Expected events for $1.5\,\mathrm{ab}^{-1}$	Simulated events	Generator level cut efficiency (%)	σ(fb)	Expected events in $1.5\,\mathrm{ab}^{-1}$	Simulated events
$e^+e^- \to \nu_e\bar{\nu}_e q\bar{q}\gamma$	120.7	181050		30.9	37.30	55944	194964
$e^+e^- \to \nu_e\bar{\nu}_e q\bar{q}$	787.8	1181625		15.5	121.81	182709	162616
$e^+e^- \to \nu_e\bar{\nu}_e l^+l^-\gamma$	187.3	281004		5.1	9.61	14409	1803981
$e^+e^- \to \nu_e\bar{\nu}_e l^+l^-$	2163.7	3245475		1.1	23.32	34981	343016
$e^+e^- \to l^+l^-l^+l^-$	7089.9	10634880		1.2	85.20	127795	133916
$e^+e^- \to q\bar{q}l^+l^-\gamma$	136.0	204000		13.4	18.22	27336	38922
$e^+e^- \to q\bar{q}l^+l^-$	2725.9	4088835		3.5	95.63	143447	722725
$e^+e^- \to q\bar{q}^\dagger$	4009.5	6014250	701961				
$e^+e^- \to q\bar{q}q\bar{q}^\dagger$	1328.1	1992150	251138				
$e^+e^- \to H\nu_e\bar{\nu}_e; H \to \gamma\gamma^\dagger$	0.56	842	53500				
$e^+e^- \to H\nu_e\bar{\nu}_e; H \to \tau^+\tau^-\gamma^\dagger$	0.014	21	170263				

Table 3: Cross section and expected and simulated number of background events for an integrated luminosity of $1.5\,\text{ab}^{-1}$ $e^{\pm}\gamma$ collisions with photons from EPA and for $1.125\,\text{ab}^{-1}$ $e^{\pm}\gamma$ collisions with photons from BS which produce similar visible final state particles as the $H \to Z\gamma$ processes. All processes except those marked with a dagger (†) are simulated after applying generator level cuts. For all channels, additional final state photons are produced as ISR.

	Without cuts				With generator level cuts		
Process (γ from BS) (- ISR)	σ(fb)	Expected events for $1.125\,\text{ab}^{-1}$	Simulated events	Generator level cut efficiency (%)	σ(fb)	Expected events for $1.125\,\text{ab}^{-1}$	Simulated events
$e^{\pm}\gamma \to e^{\pm}l^{+}l^{-}\gamma$	3856.4	4338		2.2	83.10	93487	147658
$e^{\pm}\gamma \to e^{\pm}l^{+}l^{-}$	43215.4	48617325		1.3	572.83	644436	574361
$e^{\pm}\gamma \to e^{\pm}l^{+}l^{-}q\bar{q}$	35.8	40322		5.8	2.08	2335	26000
$e^{\pm}\gamma \to e^{\pm}q\bar{q}\gamma$	1296.5	1458563		7.9	103.07	115948	156812
$e^{\pm}\gamma \to e^{\pm}q\bar{q}$	20971.2	23592600		4.1	864.14	972160	732949
$e^{\pm}\gamma \to e^{\pm}q\bar{q}\nu_e\bar{\nu}_e$	30.1	33863		15.4	4.77	5382	38606
$e^{\pm}\gamma \to e^{\pm}q\bar{q}q\bar{q}^{\dagger}$	2317.3	2606963	759592				
	Without cuts				With generator level cuts		
Process (γ from EPA) (- ISR)	σ(fb)	Expected events for $1.5\,\text{ab}^{-1}$	Simulated events	Generator level cut efficiency (%)	σ(fb)	Expected events for $1.5\,\text{ab}^{-1}$	Simulated events
$e^{\pm}\gamma \to e^{\pm}l^{+}l^{-}\gamma$	1557.9	2336850		5.5	86.04	129057	150612
$e^{\pm}\gamma \to e^{\pm}l^{+}l^{-}$	39598.8	59398200		3.5	1369.23	2053841	1477860
$e^{\pm}\gamma \to e^{\pm}l^{+}l^{-}q\bar{q}$	9.9	14822		10.2	1.01	1509	23057
$e^{\pm}\gamma \to e^{\pm}q\bar{q}\gamma$	493.5	740250		12.3	60.85	91270	108699
$e^{\pm}\gamma \to e^{\pm}q\bar{q}$	14962.1	22443150		7.4	1113.71	1670568	1604943
$e^{\pm}\gamma \to e^{\pm}q\bar{q}\nu_e\bar{\nu}_e$	6.6	9900		20.0	1.33	1995	29426
$e^{\pm}\gamma \to e^{\pm}q\bar{q}q\bar{q}^{\dagger}$	574.0	861000	798367				

3. Photon reconstruction in CLIC_SiD_CDR

The studies of the $H \to Z\gamma$ and the $H \to \gamma\gamma$ decay channels are the first physics benchmark-studies at CLIC performed with the CLIC_SiD_CDR detector concept that require excellent photon reconstruction. In the following, the quality of the photon reconstruction for the CLIC_SiD_CDR detector concept is tested. First, the photon reconstruction and identification efficiency and the agreement between the generated and the reconstructed photon properties are studied. Then, optimisations in the photon reconstruction for future benchmark studies are discussed.

3.1. Reconstruction and identification efficiency

The reconstruction and identification efficiency is defined as

$$\varepsilon_\gamma = \frac{N_{\text{particles, reconstructed and correctly identified}}}{N_{\text{particles, generated}}}. \tag{1}$$

Figures 3(a) and 3(b) show the photon reconstruction and identification efficiency as a function of the generated transverse momentum $p_{\text{T, gen}}$ and as a function of the generated polar angle θ_{gen}. The efficiencies are estimated for photons from the $H \to Z\gamma$ signal sample using only photons originating from the Higgs decay. The mean energy of these photons is $\langle E_\gamma \rangle = 60\,\text{GeV}$. The energy and the transverse momentum distributions of the signal photons are shown in Appendix A, Figures 19 and 20.
The mean efficiency for all photons of the signal sample for $p_{\text{T, gen}} > 5\,\text{GeV}$ and $10^\circ < \theta_{\text{gen}} < 170^\circ$ is $\langle \varepsilon_\gamma \rangle = 97.4\%$. It increases as a function of the transverse momentum. In the lowest bin at $5\,\text{GeV} < p_{\text{T, gen}} < 10\,\text{GeV}$, the efficiency is lowest and has a value of 93.3% in the considered θ_{gen} range. The photon reconstruction efficiency varies by 3% as a function of the polar angle ($p_{\text{T, gen}} > 5\,\text{GeV}$). In the transition region between the barrel and the end caps at approximately 37° and 143°, a decrease of the reconstruction efficiency of 1.5% can be observed. At approximately 30° and 150°, the efficiency has a maximal value of approximately 99%. It decreases to its lowest value of approximately 96% at central polar angles ($\theta_{\text{gen}} = 90^\circ$) and close to the beam directions ($\theta_{\text{gen}} = 0^\circ$ and $\theta_{\text{gen}} = 180^\circ$). The efficiency is independent of the azimuthal angle φ (figure not shown).
Of the 2.6% of photons which are not found in the reconstruction and identification, 2.5% are in fact reconstructed but misidentified; 1.9% are reconstructed as neutrons, 0.5% as electrons, and 0.1% as pions. The impact of a possible improvement of the photon identification on the final analysis results is discussed in Section 7.2.

3.2. Resolution

The resolution of a variable is defined as the width of the distribution of the differences between the reconstructed value and the generated value. The resolution for the energy E, the transverse momentum p_T, the azimuthal angle φ, and the polar angle θ for photons from the $H \to Z\gamma$ signal sample are discussed in the following.
Figure 4(a) shows the relative photon energy resolution. The mean position of the distribution is compatible with zero. The width of the distribution, estimated with a Gaussian fit with a $\pm 1.5\sigma$ fit range, is $\sigma = (3.33 \pm 0.01)\%$. In Figure 4(b), the relative transverse momentum resolution is displayed. The distribution is centred at zero. The width, estimated with a Gaussian fit, is $\sigma = (3.51 \pm 0.02)\%$. Figure 4(c) shows the resolution of the azimuthal angle φ and Figure 4(d) shows the resolution of the polar angle θ. On average, the reconstructed value and the generated value of the azimuthal and polar angle agree. An improvement of the width of the polar angle resolution is discussed in the following section.

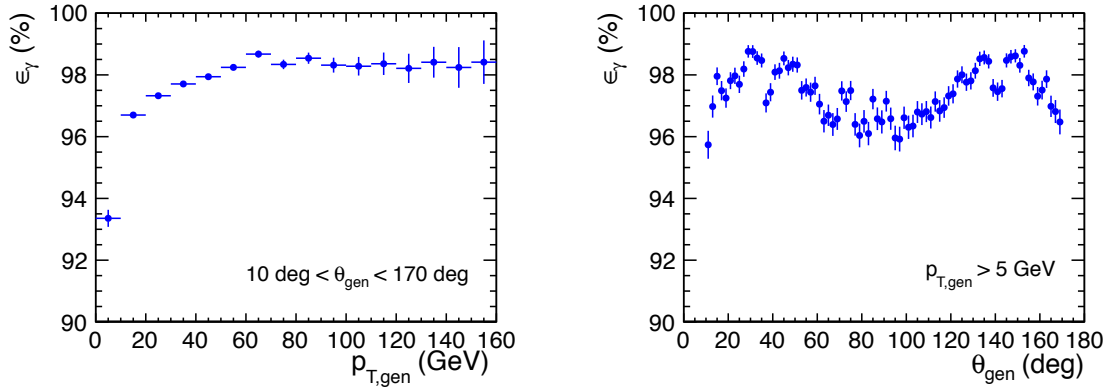

(a) (b)

Figure 3: Photon reconstruction and identification efficiency ε_γ as a function of the generated transverse momentum $p_{\mathrm{T,\,gen}}$ (a) and as a function of the generated polar angle θ_{gen} (b). Photons from the signal sample $\mathrm{H} \to \mathrm{Z}\gamma$ are used. For a better visibility, the y-axis range in both figures is limited to $90 - 100\%$.

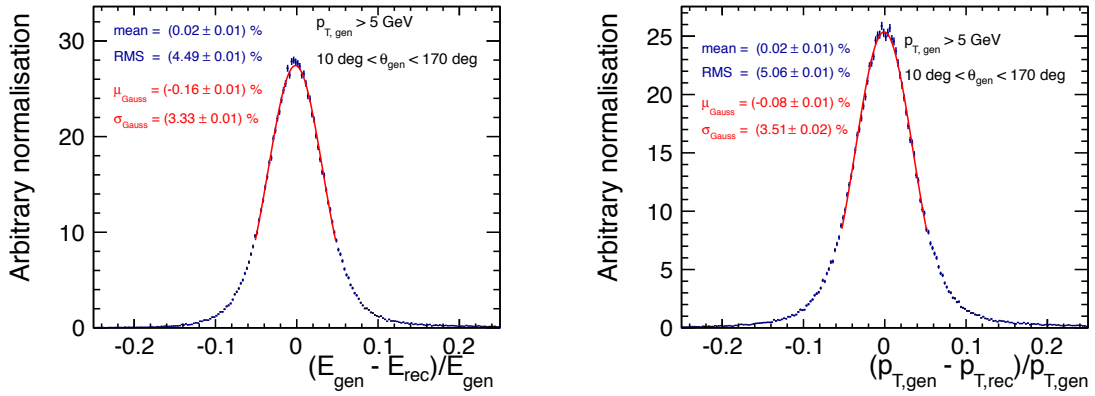

(a) (b)

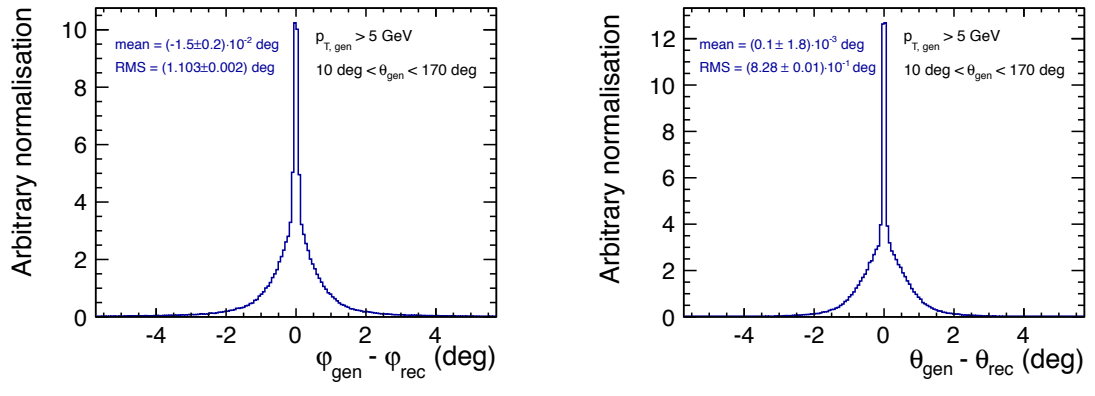

(c) (d)

Figure 4: Difference between the generated and the reconstructed photon properties energy E (a), transverse momentum p_{T} (b), azimuthal angle φ (c), and polar angle θ (d). Photons from the signal sample $\mathrm{H} \to \mathrm{Z}\gamma$ are used.

3.3. Future improvement in photon reconstruction

Photons are reconstructed in the CLIC_SiD_CDR detector model mostly using the energy deposited in the electromagnetic calorimeter (ECAL). For each calorimeter cell which detects a fraction of the photon-induced particle shower, so-called hits are recorded. From all calorimeter hits in the same detector region a cluster is formed. The position of the cluster is defined by the centre-of-gravity of all hits. The cluster position and energy together with the collision vertex position, estimated with tracks from charged particles of the same collision event, are then used to reconstruct the four-momentum vector of the photon. In the default cluster reconstruction used in this study (PANDORAPFANEW version 00-06), the cluster position is estimated using the average position of all hits only in the first calorimeter layer. If a photon does not enter the calorimeter perpendicularly, the average position of the hits can differ from the true entrance point of the photon trajectory in the calorimeter.
For the barrel in which the ECAL cells are arranged in line with the beam direction, the reconstructed cluster position can therefore be shifted along the beam direction. For the end-caps in which the calorimeter cells are arranged perpendicular to the beam direction, the reconstructed cluster position can be shifted towards central θ. An unbiased polar angle reconstruction is only achieved for photons which enter the calorimeter perpendicularly, i. e. at $\theta = 90^\circ$ or at $\theta = 0^\circ$ and 180°.
In the following, the polar angle resolution is computed for four different photon reconstruction methods; the default photon reconstruction from PANDORAPFANEW version 00-06, a photon reconstruction which uses unweighted photon hits from all calorimeter layers, and two options of hit energy weighted photon reconstructions[3]. In the first case, the hit energy itself is used as hit weight. In the second case, the hit weight, w_{hit}, is given by

$$w_{\text{hit}} = \text{Max}\left[0, C + \log\left(\frac{E_{\text{hit}}}{E_{\text{cluster}}}\right)\right] \tag{2}$$

where E_{hit} is the energy of a ECAL hit and E_{cluster} is the energy of a reconstructed photon cluster. The latter energy-weighting scheme is motivated by the fact that the hit energy distribution in the photon shower tail falls exponentially as a function of the hit energy [24]. It also allows to cut off low energy hits which could be induced by detector noise. The best polar angle resolution is achieved with the log-weighted method using $C = 4.5$.
Figure 5(a) shows that the difference between the reconstructed and the generated polar angle can be reduced when using hit energy weights in the centre-of-gravity calculation for the cluster position.
Figure 5(b) shows that the reconstruction of Higgs particles in the $H \to Z\gamma$ channel can also be improved slightly with the optimised photon reconstruction; the Higgs peak width is reduced by approximately 4% when using logarithmic hit energy weights in comparison to the default reconstruction. However, it is not expected that this improved photon reconstruction significantly affects the analysis results in terms of the precision of the cross section times branching ratio measurement. In the presented $H \to Z\gamma$ study, the uncorrected photon polar angle reconstruction is used. For future analyses, the photon reconstruction will be performed with an improved method using hit energy weights as implemented in PANDORAPFANEW starting from version 00-09.

[3] Thanks to André Sailer for identifying the source of the imperfect photon reconstruction and for pointing us to algorithms for an optimised photon reconstruction.

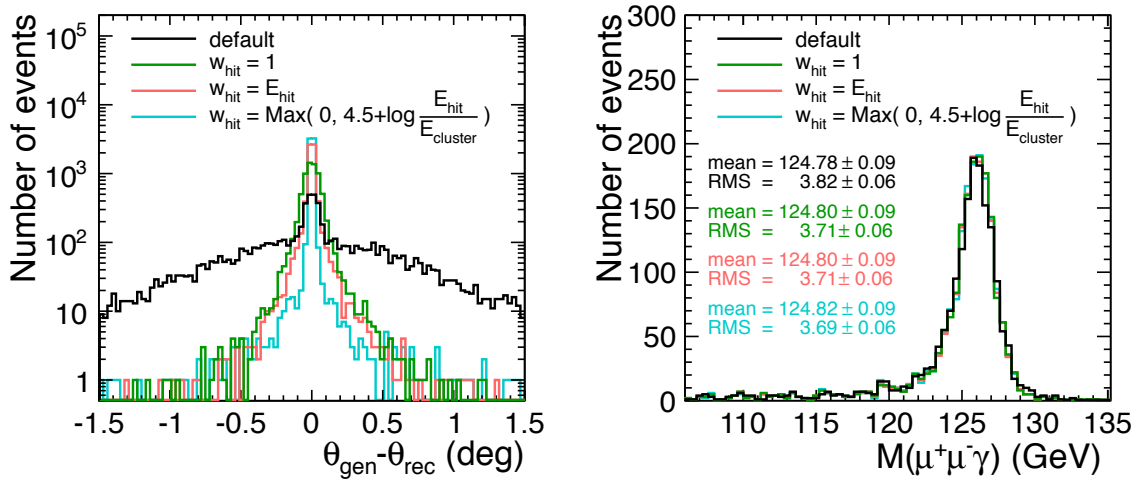

(a) (b)

Figure 5: Difference between the generated polar angle θ_{gen} and the reconstructed polar angle θ_{rec} for photons from the $H \to Z\gamma$ signal sample (a). Reconstructed Higgs mass from $H \to Z\gamma$; $Z \to \mu^+\mu^-$ events with $M_{H,\text{gen}} = 126\,\text{GeV}$ (b). Both figures show results for different photon reconstruction methods, as indicated in the figures.

4. Analysis method

This section describes the analysis algorithm for the reconstruction of Higgs candidates in the $H \to Z\gamma$ channel. The algorithm is optimised for signal events. In addition to the algorithm, the choice of the so-called timing cuts, the jet radius, and the opening angle between leptons and photons from bremsstrahlung are discussed.

A free parameter in the reconstruction is the choice of the timing cuts [8]. In order to suppress particles from $\gamma\gamma \to$ hadron pileup events which can distort the reconstructed Higgs properties, combined timing and transverse momentum cuts are applied after the reconstruction. These cuts depend on the particle type, the transverse momentum and the detector region. The full definition of the cuts can be found in [8]. Three sets of cuts can be chosen; tight, default, and loose.

In the following, the Higgs reconstruction is performed with all three timing cuts. In a later step, the best combination of timing cut and jet clustering radius or opening angle between leptons and photons is identified.

4.1. Reconstruction algorithm

As a first step in the Higgs candidate reconstruction in the $H \to Z\gamma$ decay, the photon with the highest energy in the collision event is identified. This photon is used as Higgs daughter candidate.

Then, the reconstruction of the Z candidate is performed. First, one checks whether the event contains either a e^+e^- pair or a $\mu^+\mu^-$ pair. If more than two $e^\pm$ or two $\mu^\pm$ are found, the two most energetic $e^\pm/\mu^\pm$ are selected. If neither a e^+e^- pair nor a $\mu^+\mu^-$ pair is found, all reconstructed particles, except the photon of highest energy, are clustered into two jets assuming that the Z decayed into two quarks. From the selected Z daughter candidates, a Z candidate is reconstructed. The highest energy photon and the Z candidate are then combined to a Higgs candidate.

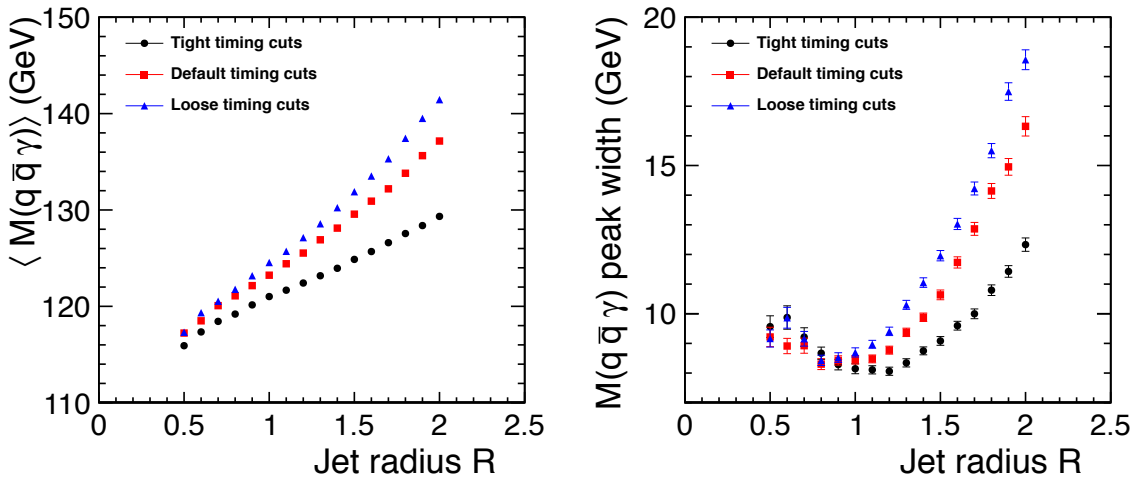

(a) (b)

Figure 6: The mean value of the reconstructed Higgs peak (a) and the width of the reconstructed Higgs peak (b) for $H \to Z\gamma; Z \to q\bar{q}$ events which are overlayed with $\gamma\gamma \to$ hadron pileup events, as a function of the jet radius. The Higgs candidates are reconstructed using different timing cuts, as indicated in the figure (see text for definition).

4.2. Quark channel $H \to Z\gamma;\ Z \to q\bar{q}$

For the case in which the Z decays into quark-antiquark pairs, the quarks hadronise and form jets. The jet reconstruction is performed with the k_T-algorithm including beam jets, as implemented in FastJet [25, 26]. As the Z decays predominantly into two quarks in the hadronic channel, the jet reconstruction is performed in exclusive mode forcing all available particles, except the highest energy photon, into two jets.

A free parameter in the jet reconstruction algorithm is the jet radius $R = \sqrt{\Delta\varphi^2 + \Delta y^2}$. The smaller the jet radius, the more likely it is to loose particles originating from the initial quark. On the other hand, the larger the jet radius, the more particles from beam-induced backgrounds or other jets can be assigned to the jet by mistake.

The reconstructed Higgs mass and width is shown in Figure 6 for the $H \to Z\gamma; Z \to q\bar{q}$ signal events overlayed with $\gamma\gamma \to$ hadron pileup events for the three timing cuts, using different values for the jet radius. The Higgs mass and width are extracted using a Gaussian fit with a fit range of $\pm 1.5\sigma$.

It can be seen that the Higgs peak width of the $Z \to q\bar{q}$ channel is smallest for tight timing cuts and a jet radius of $R = 1.2$. In the following analysis, these settings are used for the quark channel. It has to be noted, that the Higgs mass is underestimated with these reconstruction settings. It has a mean value of $M(q\bar{q}\gamma) = (122.42 \pm 0.09)\,\text{GeV}$.

4.3. Electron and muon channels $H \to Z\gamma;\ Z \to e^+e^-/\mu^+\mu^-$

When traversing the detector material, electrons and also muons can radiate photons via the bremsstrahlung process. In order to recuperate the initial lepton energy, those photons have to be identified and recombined with the leptons. Photons coming from bremsstrahlung are mostly collinear with respect to the initial lepton and hence can be identified by their opening angle, $\Theta(\gamma, l^{\pm})$, with respect to the lepton. The optimal choice of the maximum opening angle between the lepton and the photons can be found by minimizing the reconstructed Higgs peak width.

Figure 7 shows the mean value of the mass and the width of the reconstructed Higgs peak, extracted

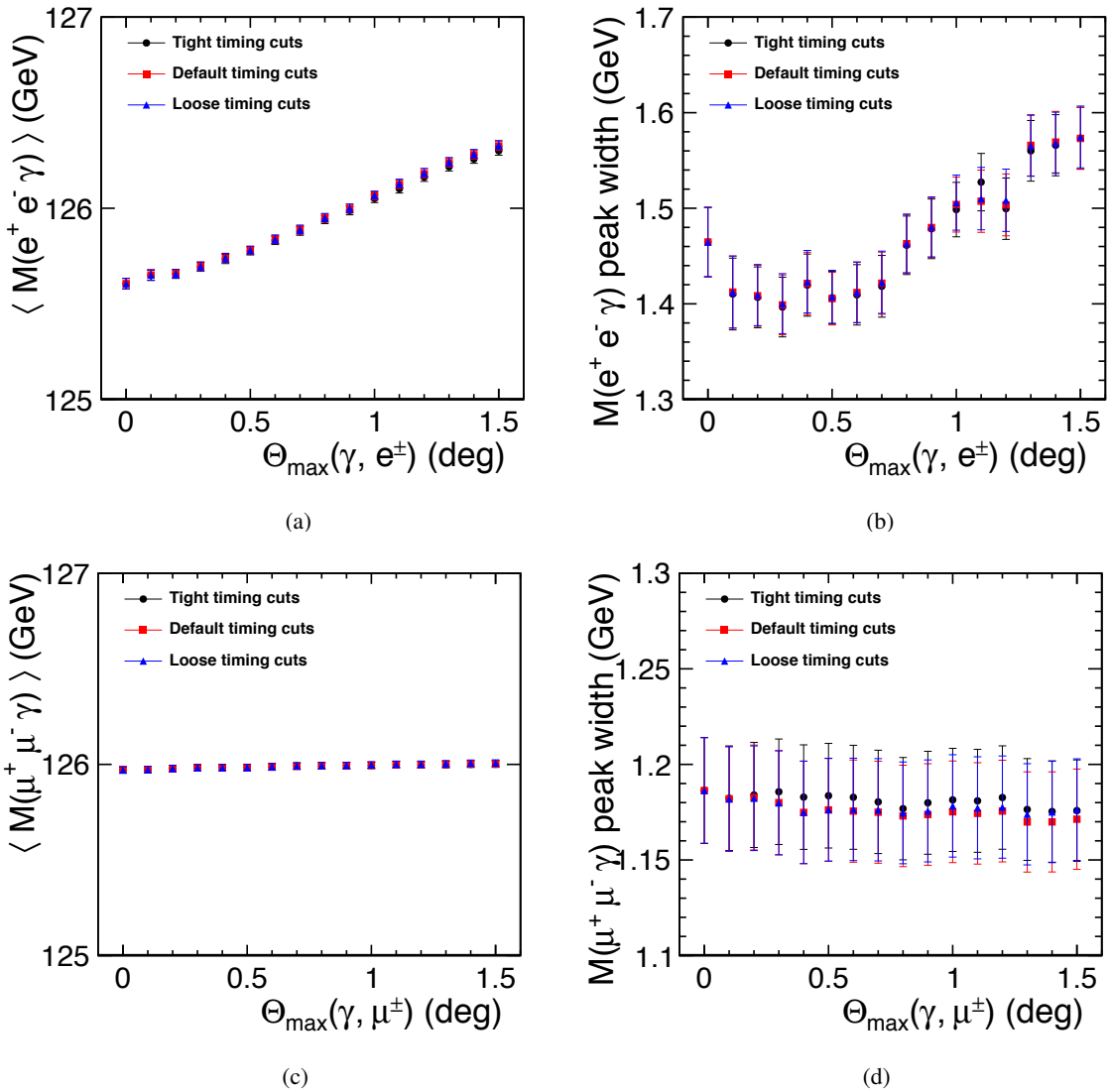

Figure 7: The mean value (a,c) and the width of the reconstructed Higgs peak (b,d) for $H \to Z\gamma; Z \to e^+e^-$ events (a,b) and for $H \to Z\gamma; Z \to \mu^+\mu^-$ events (c,d), overlayed with $\gamma\gamma \to$ hadron pileup events, as a function of the maximum opening angle $\Theta_{\max}(\gamma, l^{\pm})$. The Higgs candidates are reconstructed using different timing cuts, as indicated in the figure (see text for definition).

using Gaussian fits with a fit range of $\pm 1.5\sigma$, for electron and muon signal events as a function of the maximal allowed opening angles, $\Theta_{\max}(\gamma, l^{\pm})$, between the lepton and the photon(s).

While the correction for photons from bremsstrahlung in terms of the selection on the opening angle has an effect on the electron results (Figures 7(a) and 7(b)), the muon results remain unchanged within the statistical uncertainty (Figures 7(c) and 7(d)). This is expected, as due to their higher mass muons produce less bremsstrahlung than electrons.

As the timing cuts reduce mostly hadronic backgrounds, they are not relevant in the analysis of the leptonic Z decays as illustrated in Figure 7. For consistency with the quark channel analysis, the electron and muon channels are studied in the following also using the tight timing cuts.

The best width of the Higgs peak in the electron case can be found with a maximum opening angle of approximately $\Theta_{\max}(\gamma, e^{\pm}) = 0.3°$. At this opening angle, the reconstructed Higgs mass has a mean value of $M(e^+e^-\gamma) = (125.69 \pm 0.02)$ GeV and $M(\mu^+\mu^-\gamma) = (125.98 \pm 0.02)$ GeV.

5. Event selection

This section describes the discrimination between signal and background events based on pre-selection cuts and a multivariate analysis.

5.1. Pre-selection

In the following, the pre-selection cuts applied to all signal and background channels are described. These cuts are tighter than the generator level cuts introduced in Section 2.2 that are applied only to background processes before detector simulation and reconstruction. This ensures that the generator level cuts do not bias the analysis results. The pre-selection cuts have been optimised for a high acceptance of signal events as well as a high rejection of background events.
Only particles passing the tight time selection cuts are accepted in the analysis. The Higgs candidate daughters, the jets, leptons, and photons, are only accepted if they have an energy of $E > 20\,\text{GeV}$ and a transverse momentum of $p_\text{T} > 15\,\text{GeV}$. In the quark channel, only jets with at least 5 particles are considered in order to suppress jets containing only one lepton and jets from hadronic τ-decays. In addition, the reconstructed H and Z mass are restricted to fulfil

- $M(\text{q}\bar{\text{q}}\gamma) \quad = 122.4^{+15}_{-20}\,\text{GeV}$ and $M(\text{q}\bar{\text{q}}) \quad = 87.6^{+15}_{-20}\,\text{GeV}$,
- $M(\text{e}^+\text{e}^-\gamma) = 125.7^{+7.5}_{-10}\,\text{GeV}$ and $M(\text{e}^+\text{e}^-) = 89.9^{+7.5}_{-10}\,\text{GeV}$, or
- $M(\mu^+\mu^-\gamma) = 126.0^{+7.5}_{-10}\,\text{GeV}$ and $M(\mu^+\mu^-) = 91.2^{+7.5}_{-10}\,\text{GeV}$.

Here, the acceptance ranges are centred at the mean values of the reconstructed H and Z masses, as estimated in Section 4. As the mass distributions are asymmetric (see Appendix A, Figures 9 and 14), the accepted mass ranges are also chosen to be asymmetric. The widths of the mass ranges are motivated by the widths of the reconstructed mass peaks.
The number of signal and background events before and after pre-selection cuts are listed in Tables 4 to 6. While the pre-selection cuts accept between 40% and 50% of the signal events, the background processes can be reduced to between 0% and 12%.

5.2. Multivariate analysis

As a second step in the event selection, a classification and selection based on a multivariate data analysis is performed. First, the input variables for the multivariate analysis are introduced. Then, the multivariate analysis strategy is discussed.
As input to the multivariate analysis, kinematic properties of the reconstructed candidate events are used. The following 27 variables are analysed in all Z decay channels:

1.–2. invariant mass M of reconstructed H and Z candidates;

3.–4. velocity β of the reconstructed H and Z candidates;

5.–7. energy E of the reconstructed H, Z, and γ candidates;

8.–10. transverse momentum p_T of the reconstructed H, Z, and γ candidates;

11.–13. polar angle θ of the reconstructed H, Z, and γ candidates;

14. scalar sum $\sum |\overrightarrow{p_\text{T}}|$ of the reconstructed H candidate daughters;

15.–18. thrust, sphericity, aplanarity, and oblateness of the reconstructed H candidate daughters;

19. angle $\Theta(\mathrm{Z},\gamma)$ between vectors of the reconstructed Z and γ candidates;
20. $\Delta\theta = |\theta_{\mathrm{Z}} - \theta_{\gamma}|$ between the polar angles of the reconstructed Z and γ candidates;
21. $\Delta\varphi = \varphi_{\mathrm{Z}} - \varphi_{\gamma}$ between the azimuthal angles of the reconstructed Z and γ candidates;
22. helicity angle $\cos\theta^*(\mathrm{Z},\gamma)$ in the rest frame of the H candidate;
23. helicity angle $\cos\theta^*(\mathrm{f},\bar{\mathrm{f}})$ (with $\mathrm{f} = \mathrm{e},\mu$,jet) in the rest frame of the Z candidate;
24. visible energy excluding the reconstructed H candidate energy $E_{\mathrm{vis}} - E_{\mathrm{H}}$;

25.–26. missing energy $\not{E}$ and missing transverse energy $\not{E}_{\mathrm{T}}$ of the reconstructed Higgs daughters;

27. particle multiplicity N_{particle} ($E > 0\,\mathrm{GeV}$ and $p_{\mathrm{T}} > 0\,\mathrm{GeV}$).

In the case of a $\mathrm{Z} \to \mathrm{q\bar{q}}$ decay, five additional jet properties are used for the event classification:

1. particle multiplicity, $N_{\mathrm{Z,particle}}$, used in the Z reconstruction ($E > 0\,\mathrm{GeV}$ and $p_{\mathrm{T}} > 0\,\mathrm{GeV}$);

2.–5. $d_{n,n+1}$ value associated with the merging from n to $n+1$ jets with $n = \{1-4\}$.

All discussed kinematic variables are shown for signal and background channels for the three Z decay channels in Appendix A, Figures 9-37. The most powerful variables to distinguish between signal and background processes are M_{H} (Figure 9), $p_{\mathrm{T,H}}$ (Figure 12), $\sum|\overrightarrow{p_{\mathrm{T}}}|$ (Figure 22), $\cos\theta^*(\mathrm{f},\bar{\mathrm{f}})$ (Figure 31), $E_{\mathrm{vis}} - E_{\mathrm{H}}$ (Figure 32), and $\not{E}_{\mathrm{T}}$ (Figure 34).

Boosted decision trees (BDT) as implemented in the toolkit for multivariate data analysis (TMVA) [27] are used to identify signal and background processes. The training of the BDTs is performed based on the kinematic variables introduced before.
For each of the studied H decay channels, an independent BDT with adaptive boosting and 400 decisions trees is used. The trees are trained using half of the available signal and background events. After that, the remaining second half of events is analysed with the trained BDT. In this step, a classifier called BDT response is calculated for each event.
On average, signal and signal-like events are assigned with a BDT response larger than zero, while background events are assigned with a BDT response smaller than zero. With a selection on the BDT response in the vicinity of zero, it is possible to select a large fraction of all signal events while rejecting a large fraction of all background events. In the following, a lower limit of the BDT response is chosen which results in the highest significance, defined as

$$\text{Significance} = \frac{N_{\text{evt, sig}}}{\sqrt{N_{\text{evt, sig}} + N_{\text{evt, bkg}}}}, \tag{3}$$

where $N_{\text{evt, sig}}$ is the number of signal events and $N_{\text{evt, bkg}}$ is the number of background events. In the subsequent analysis steps, only events are used which have a BDT response above the BDT value which results in the highest significance.

6. Results

When trying to extract the number of signal and background events in the analysis of a particle decay, there are two common approaches to present the analysis results. In the first approach, the number of signal and background events are extracted from the invariant Higgs mass distribution after BDT selection using a fit function. This fit function describes the expected shape of the invariant mass distribution including a mass peak for the signal events and a flat mass distribution for the background events. In order not to bias the background "Higgs mass" distribution, the multivariate event selection has to be performed without the particle's invariant mass as an input variable. In the second approach, the particle's mass is used in the BDT event classification. Hence, the background mass distribution resembles the signal mass distribution after BDT selection which makes it impossible to extract the number of signal and background events using a fit function. Therefore, the number of signal and background events after BDT selection are counted using the Monte Carlo truth information.
For the process $e^+e^- \to H\nu_e\bar{\nu}_e; H \to Z\gamma$, both approaches have been tested. However, due to the low number of signal events after BDT selection, the first approach, in which the number of signal events is extracted from the Higgs invariant mass distribution using a fit function, turned out not to be feasible. It was not possible to identify a clear Higgs mass peak on top of the flat background, as shown in Figure 39 in Appendix B. This approach is suitable only for studies of particle decays with much larger signal to background ratios than the studied $H \to Z\gamma$ decay. Hence, only the second approach of the counting experiment is discussed.

In the following, the H and Z mass and energy are included in the BDT event classification. Figures 8(a), 8(c), and 8(e) show the BDT response for signal and background events. The significance, as well as the signal and the background efficiencies, are shown in Figures 8(b), 8(d), and 8(f), as a function of the BDT selection.
Using the H and Z mass and energy in the BDT event classification, the significance increases with respect to the case where they are not used (compare Figure 8 and Figure 38 from Appendix B). The maximal significance for the quark, electron, and muon channels and the corresponding BDT selection are

- $\text{Significance}_{H\to Z\gamma;Z\to q\bar{q}} = 2.20$ at $\text{BDT}_{H\to Z\gamma;Z\to q\bar{q}} = 0.14$,
- $\text{Significance}_{H\to Z\gamma;Z\to e^+e^-} = 0.54$ at $\text{BDT}_{H\to Z\gamma;Z\to e^+e^-} = 0.14$,
- $\text{Significance}_{H\to Z\gamma;Z\to \mu^+\mu^-} = 0.78$ at $\text{BDT}_{H\to Z\gamma;Z\to \mu^+\mu^-} = 0.15$.

The number of events for the signal and background processes after BDT selection are listed in Tables 4 to 6. While the BDT selection accepts between 17% and 25% of the signal events, the background processes can be reduced to between 0% and 1%.
The distributions of all kinematic variables for events that pass the BDT selection are shown in Appendix A in Figures 9-37 in comparison to the same distributions before BDT selection. The most important background channels which can not be removed completely by pre-selection cuts and the BDT selection, are $e^+e^- \to \nu_e\bar{\nu}_e q\bar{q}(\gamma)$ and $e^\pm\gamma \to e^\pm q\bar{q}$ in the quark channel and $e^+e^- \to \nu_e\bar{\nu}_e l^+l^-(\gamma)$ and $e^\pm\gamma \to e^\pm l^+l^-$ in the lepton channels. The difference in the results of the $H \to Z\gamma; Z \to e^+e^-$ channel and the $H \to Z\gamma; Z \to \mu^+\mu^-$ channel is discussed in Section 7.3.
As the three channels are independent, the significances of the three channels are combined in quadrature and the combined significance has a value of 2.40. The significance can be transformed into the statistical uncertainty of the cross section times branching ratio measurement, resulting in

$$\delta(\sigma_{e^+e^-\to H\nu_e\bar{\nu}_e} \times \text{BR}_{H\to Z\gamma}) = \frac{1}{\text{Significance}_{\text{combined}}} = \frac{1}{2.40} = 0.417. \tag{4}$$

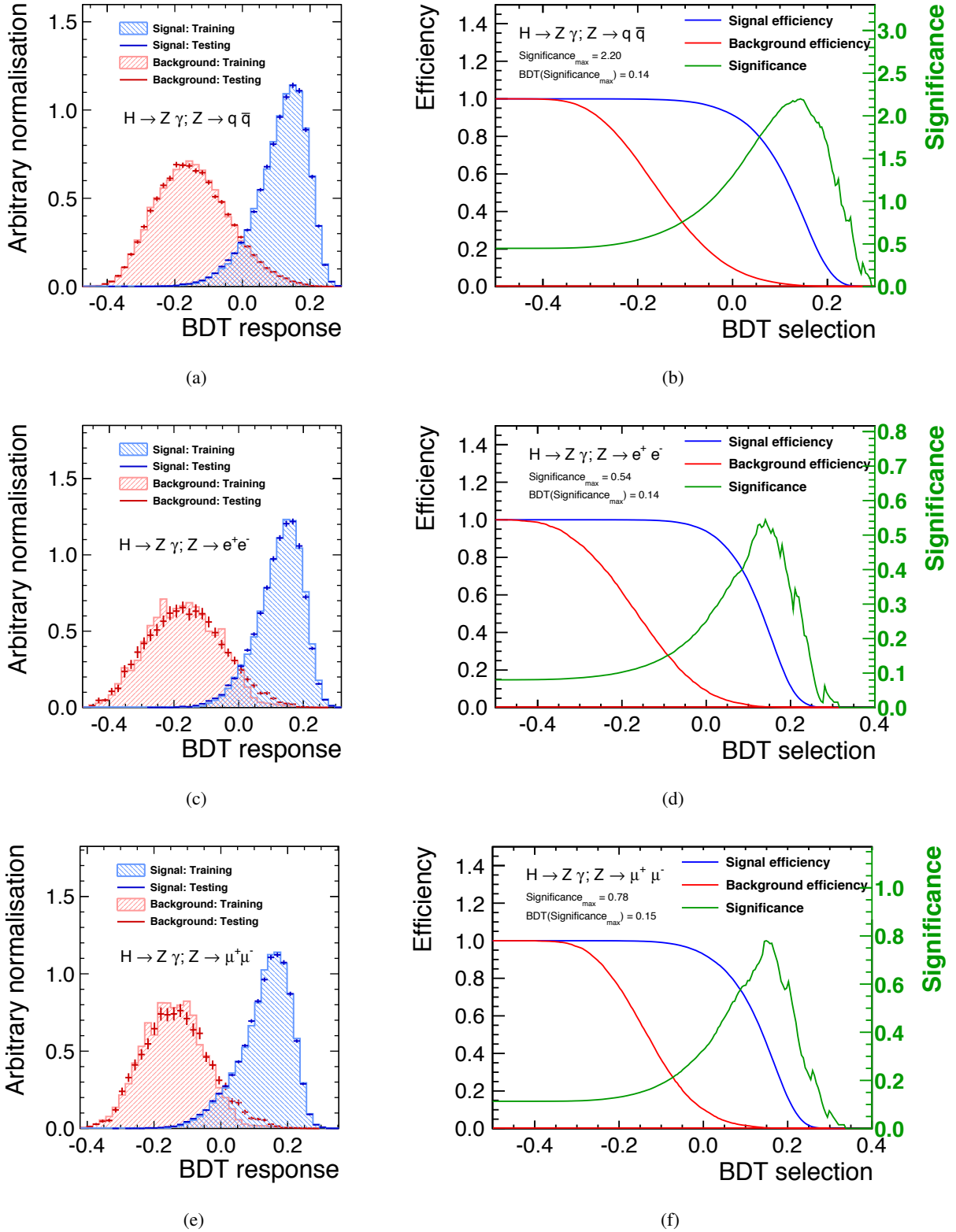

Figure 8: BDT response for signal events (blue) and background events (red) based on kinematic variables introduced in Section 5.2 (a,c,e) and the significance, the signal and the background efficiencies, as a function of the BDT selection (b,d,f) for the $H \to Z\gamma; Z \to q\bar{q}$ channel (a,b), the $H \to Z\gamma; Z \to e^+e^-$ channel (c,d), and the $H \to Z\gamma; Z \to \mu^+\mu^-$ channel (e,f). The maximum significance found per channel and the corresponding BDT selection cut are indicated in the figures (b,d,f).

In comparison to the estimated statistical precision of the $\sigma_{e^+e^-\to H\nu_e\bar{\nu}_e} \times BR_{H\to Z\gamma}$ measurement, systematic uncertainties, for example, from the luminosity uncertainty, detector effects, and the jet energy scale uncertainty are expected to be negligible.
This statistical uncertainty $\delta(\sigma_{e^+e^-\to H\nu_e\bar{\nu}_e} \times BR_{H\to Z\gamma})$ estimated in this study is similar to those predicted for measurements at the High-Luminosity LHC at an integrated luminosity of $3\,ab^{-1}$ of proton–proton collisions at $\sqrt{s} = 14\,TeV$ [28, 29].

Table 4: Number of signal and background events for the $H \to Z\gamma; Z \to q\bar{q}$ channel at $\sqrt{s} = 1.4\,TeV$ expected for $1.5\,ab^{-1}$ for the initial states e^+e^- and $e^\pm\gamma$ (EPA) and for $1.125\,ab^{-1}$ for the initial state $e^\pm\gamma$ (BS). The initial state processes $e^\pm\gamma$ from BS or from EPA are combined. The first column indicates the process, the second column shows the number of events after generator level (g.l.) cuts (processes marked with a dagger, †, are simulated without g.l. cuts), the third column shows the number of events after pre-selection, and the last column the number of events after BDT selection. In the last two columns, also the fraction of events that pass the selection step with respects to the number of events after g.l. cuts are indicated.

Process	Events after g.l. cuts	Events after pre-sel.	(%)	Events after BDT sel.	(%)
$e^+e^- \to H\nu_e\bar{\nu}_e; H \to Z\gamma; Z \to q\bar{q}^\dagger$	409	184	(45.07)	75	(18.22)
$e^+e^- \to H\nu_e\bar{\nu}_e; H \to Z\gamma; Z \to e^+e^{-\dagger}$	21	0	(0.00)	0	(0.00)
$e^+e^- \to H\nu_e\bar{\nu}_e; H \to Z\gamma; Z \to \mu^+\mu^{-\dagger}$	21	0	(0.00)	0	(0.00)
$e^+e^- \to H\nu_e\bar{\nu}_e; H \to Z\gamma; Z \to \tau^+\tau^{-\dagger}$	21	1	(4.76)	0	(0.00)
$e^+e^- \to H\nu_e\bar{\nu}_e; H \to \gamma\gamma^\dagger$	842	0	(0.00)	0	(0.00)
$e^+e^- \to \nu_e\bar{\nu}_e q\bar{q}\gamma$	55944	6894	(12.32)	504	(0.90)
$e^+e^- \to \nu_e\bar{\nu}_e q\bar{q}$	182709	15332	(8.39)	463	(0.24)
$e^+e^- \to q\bar{q}^\dagger$	6014250	17187	(0.29)	0	(0.00)
$e^+e^- \to q\bar{q}q\bar{q}^\dagger$	1992150	6774	(0.34)	0	(0.00)
$e^+e^- \to \nu_e\bar{\nu}_e l^+l^-\gamma$	13038	179	(1.37)	1	(0.01)
$e^+e^- \to \nu_e\bar{\nu}_e l^+l^-$	34981	349	(1.00)	2	(0.01)
$e^+e^- \to l^+l^-l^+l^-$	127795	1504	(1.18)	2	(<0.01)
$e^+e^- \to q\bar{q}l^+l^-\gamma$	27336	535	(1.96)	0	(0.00)
$e^+e^- \to q\bar{q}l^+l^-$	143447	4149	(2.89)	6	(<0.01)
$e^\pm\gamma \to e^\pm q\bar{q}$	2642728	63462	(2.40)	70	(<0.01)
$e^\pm\gamma \to e^\pm q\bar{q}q\bar{q}^\dagger$	3467963	34373	(0.79)	2	(<0.01)
$e^\pm\gamma \to e^\pm l^+l^-$	2698277	9327	(0.35)	7	(<0.01)
$e^\pm\gamma \to e^\pm q\bar{q}\nu_e\bar{\nu}_e$	7377	318	(4.31)	8	(0.11)
$e^\pm\gamma \to e^\pm l^+l^-\gamma$	222544	1485	(0.67)	1	(<0.01)
$e^\pm\gamma \to e^\pm q\bar{q}\gamma$	207218	6652	(3.21)	6	(<0.01)
$e^\pm\gamma \to e^\pm l^+l^-q\bar{q}$	3844	116	(3.02)	0	(0.00)

Table 5: Same as Table 4 for the $H \to Z\gamma; Z \to e^+e^-$ channel.

Process	Events after g.l. cuts	Events after pre-sel.	(%)	Events after BDT sel.	(%)
$e^+e^- \to H\nu_e\bar{\nu}_e; H \to Z\gamma; Z \to e^+e^{-\dagger}$	21	8	(38.26)	4	(17.34)
$e^+e^- \to H\nu_e\bar{\nu}_e; H \to Z\gamma; Z \to q\bar{q}^\dagger$	409	0	(0.00)	0	(0.00)
$e^+e^- \to H\nu_e\bar{\nu}_e; H \to Z\gamma; Z \to \mu^+\mu^{-\dagger}$	21	0	(0.00)	0	(0.00)
$e^+e^- \to H\nu_e\bar{\nu}_e; H \to Z\gamma; Z \to \tau^+\tau^{-\dagger}$	21	0	(0.00)	0	(0.00)
$e^+e^- \to H\nu_e\bar{\nu}_e; H \to \gamma\gamma^\dagger$	842	0	(0.00)	0	(0.00)
$e^+e^- \to \nu_e\bar{\nu}_e q\bar{q}\gamma$	55944	0	(0.00)	0	(0.00)
$e^+e^- \to \nu_e\bar{\nu}_e q\bar{q}$	182709	0	(0.00)	0	(0.00)
$e^+e^- \to q\bar{q}^\dagger$	6014250	223	(<0.01)	0	(0.00)
$e^+e^- \to q\bar{q}q\bar{q}^\dagger$	1992150	111	(0.01)	0	(0.00)
$e^+e^- \to \nu_e\bar{\nu}_e l^+l^-\gamma$	14409	225	(1.56)	15	(0.10)
$e^+e^- \to \nu_e\bar{\nu}_e l^+l^-$	34981	360	(1.03)	12	(0.03)
$e^+e^- \to l^+l^-l^+l^-$	127795	296	(0.23)	4	(<0.01)
$e^+e^- \to q\bar{q}l^+l^-\gamma$	27336	25	(0.09)	0	(0.00)
$e^+e^- \to q\bar{q}l^+l^-$	143447	94	(0.07)	0	(0.00)
$e^\pm\gamma \to e^\pm q\bar{q}$	2642728	924	(0.04)	0	(0.00)
$e^\pm\gamma \to e^\pm q\bar{q}q\bar{q}^\dagger$	3467963	239	(0.01)	0	(0.00)
$e^\pm\gamma \to e^\pm l^+l^-$	2698277	5887	(0.22)	7	(<0.01)
$e^\pm\gamma \to e^\pm q\bar{q}\nu_e\bar{\nu}_e$	7377	10	(0.14)	0	(0.00)
$e^\pm\gamma \to e^\pm l^+l^-\gamma$	222544	1428	(0.64)	3	(<0.01)
$e^\pm\gamma \to e^\pm q\bar{q}\gamma$	207218	109	(0.05)	0	(0.00)
$e^\pm\gamma \to e^\pm l^+l^-q\bar{q}$	3844	9	(0.23)	0	(0.00)

Table 6: Same as Table 4 for the $H \to Z\gamma; Z \to \mu^+\mu^-$ channel.

Process	Events after g.l. cuts	Events after pre-sel.	(%)	Events after BDT sel.	(%)
$e^+e^- \to H\nu_e\bar{\nu}_e; H \to Z\gamma; Z \to \mu^+\mu^{-\dagger}$	21	11	(53.74)	5	(24.52)
$e^+e^- \to H\nu_e\bar{\nu}_e; H \to Z\gamma; Z \to q\bar{q}^{\dagger}$	409	0	(0.00)	0	(0.00)
$e^+e^- \to H\nu_e\bar{\nu}_e; H \to Z\gamma; Z \to e^+e^{-\dagger}$	21	0	(0.00)	0	(0.00)
$e^+e^- \to H\nu_e\bar{\nu}_e; H \to Z\gamma; Z \to \tau^+\tau^{-\dagger}$	21	0	(0.00)	0	(0.00)
$e^+e^- \to H\nu_e\bar{\nu}_e; H \to \gamma\gamma^{\dagger}$	842	0	(0.00)	0	(0.00)
$e^+e^- \to \nu_e\bar{\nu}_e q\bar{q}\gamma$	55944	0	(0.00)	0	(0.00)
$e^+e^- \to \nu_e\bar{\nu}_e q\bar{q}$	182709	0	(0.00)	0	(0.00)
$e^+e^- \to q\bar{q}^{\dagger}$	6014250	34	(<0.01)	0	(0.00)
$e^+e^- \to q\bar{q}q\bar{q}^{\dagger}$	1992150	0	(0.00)	0	(0.00)
$e^+e^- \to \nu_e\bar{\nu}_e l^+l^-\gamma$	14409	177	(1.23)	14	(0.10)
$e^+e^- \to \nu_e\bar{\nu}_e l^+l^-$	34981	157	(0.45)	13	(0.04)
$e^+e^- \to l^+l^-l^+l^-$	127795	269	(0.21)	0	(0.00)
$e^+e^- \to q\bar{q}l^+l^-\gamma$	27336	34	(0.12)	0	(0.00)
$e^+e^- \to q\bar{q}l^+l^-$	143447	25	(0.02)	0	(0.00)
$e^\pm\gamma \to e^\pm q\bar{q}$	2642728	2	(<0.01)	0	(0.00)
$e^\pm\gamma \to e^\pm q\bar{q}q\bar{q}^{\dagger}$	3467963	0	(0.00)	0	(0.00)
$e^\pm\gamma \to e^\pm l^+l^-$	2698277	7391	(0.27)	9	(<0.01)
$e^\pm\gamma \to e^\pm q\bar{q}\nu_e\bar{\nu}_e$	7377	0	(0.00)	0	(0.00)
$e^\pm\gamma \to e^\pm l^+l^-\gamma$	222544	1810	(0.81)	3	(<0.01)
$e^\pm\gamma \to e^\pm q\bar{q}\gamma$	207218	0	(0.00)	0	(0.00)
$e^\pm\gamma \to e^\pm l^+l^-q\bar{q}$	3844	11	(0.29)	0	(0.00)

7. Outlook

This section discusses the impact on the final analysis results when improving the reconstruction and identification algorithms for jets, photons and electrons used in this study, as well as the impact of performing e^+e^- collisions at CLIC using beam polarisation and a higher centre-of-mass energy.

7.1. Optimisation of jet energy resolution

The hadronic signal channel $H \to Z\gamma; Z \to q\bar{q}$ has a broader Higgs mass peak than the leptonic signal channels $H \to Z\gamma; Z \to e^+e^-/\mu^+\mu^-$. Nevertheless, the hadronic channel forms the largest contribution to the overall significance of the cross section times branching ratio measurement in this study (see Section 6). This is due to the higher number of events in the hadronic channel (409 $H \to Z\gamma; Z \to q\bar{q}$ events for an integrated luminosity of $1.5 ab^{-1}$) in comparison to the leptonic channels (21 $H \to Z\gamma; Z \to e^+e^-/\mu^+\mu^-$ events each for $1.5 ab^{-1}$).
The Higgs mass peak width in the hadronic channel is dominated by the jet energy resolution while the photon energy resolution only gives a minor contribution to the overall width. A significant improvement of the analysis results could therefore only be achieved when improving the experiment's jet energy resolution.
Simulation studies of the CLIC detector concepts, one of which was used in this study, showed that a jet energy resolution of 5%–3.5% for jets with an energy of 50 GeV to 1 TeV jets can be achieved when using high granularity calorimeters and particle flow reconstruction [8, 20]. Ongoing detector optimisation studies at CLIC currently investigate if it is possible to improve this jet energy resolution further while keeping the high granularity of the calorimeters needed for the particle flow reconstruction.

7.2. Optimisation of photon identification

The default particle reconstruction and identification used in this study is provided by the PANDORAPFA particle flow algorithm. The overall photon reconstruction and identification efficiency estimated with photons from the $H \to Z\gamma$ signal sample has a value of 97.4%. Of those photons which are not found and correctly identified in the reconstruction, approximately 75% are misidentified as neutrons, 20% as electrons, and 5% as pions. An optimised particle identification could reduce the observed misidentification. With an ideal photon reconstruction and identification efficiency of 100%, the number of reconstructed signal and background events could increase by 2.6%. This results in an improved significance by a factor of at most $\sqrt{1.026} \approx 1.013$. This corresponds to an improved combined significance of 2.43 resulting in a $\delta(\sigma_{e^+e^-\to H\nu_e\bar{\nu}_e} \times BR_{H\to Z\gamma})$ of at most 41.1%. This uncertainty is 0.6% smaller than the uncertainty estimated when using the default photon reconstruction.

7.3. Optimisation of electron identification

The difference between the significances for the signal channels $H \to Z\gamma; Z \to e^+e^-$ and $H \to Z\gamma; Z \to \mu^+\mu^-$ presented in Section 6 can be explained as follows. In Tables 5 and 6, it can be seen that only 38.26% of the signal events from the $H \to Z\gamma; Z \to e^+e^-$ channel pass the pre-selection cuts while 53.74% of the $H \to Z\gamma; Z \to \mu^+\mu^-$ events pass the pre-selection cuts. Hence, the efficiency is approximately 29% lower for the electron case than for muon case.
This is caused by a difference in the reconstruction and identification efficiency of electrons and muons in the PANDORAPFA particle flow algorithm used in this study. While the reconstruction and identification efficiency for muons is 99% for the $H \to Z\gamma$ signal events, it is only 85% for electrons. A fraction of 14% of all electrons are misidentified as pions, 1% as photons. Hence, the probability to reconstruct a lepton pair is 98% for muons and only 72% for electrons.
In addition, the reconstructed Higgs mass peak is slightly broader in the electron case than in the muon

case (cf. Figure 9 in Appendix A) due to bremsstrahlung in the electron case which is partially not recovered in the analysis algorithm. As the pre-selection cut on the Higgs mass-peak-range is similar for electrons and muons, slightly more electron events are rejected than in the muon case.
For future physics studies at CLIC, an improved electron identification will be applied. For the current study, an electron reconstruction which is as good as the muon reconstruction would improve the combined significance to at most 2.46 resulting in a $\delta(\sigma_{e^+e^-\to H\nu_e\bar{\nu}_e} \times BR_{H\to Z\gamma})$ of 40.6%. This uncertainty is 1.1% smaller then the uncertainty estimated when using the default electron reconstruction.

7.4. Beam polarisation and centre-of-mass energy

In the presented study, unpolarised electron and positron beams have been considered. The Higgs production cross section in e^+e^- collisions via W^+W^- fusion however increases as a function of the $e^\pm$ polarisation. When using -80% (left-handed) electron beam polarisation, the signal cross section increases by 80% with respect to unpolarised beams. With an additional $+30\%$ (right-handed) positron beam polarisation, the signal cross section increases by 130% with respect to unpolarised beams. The background process cross sections increase by at most the same amount. Hence, the significance of the measurement increases by at least a factor of $\sqrt{1.8}$ or $\sqrt{2.3}$ allowing for a $\delta(\sigma_{e^+e^-\to H\nu_e\bar{\nu}_e} \times BR_{H\to Z\gamma})$ of less than 31.1% or 27.5% when using the same integrated luminosity.
At $\sqrt{s} = 3$ TeV, the Higgs production cross section is 70% larger than at $\sqrt{s} = 1.4$ TeV and the luminosity of CLIC increases by a factor of 1.8 with respect to $\sqrt{s} = 1.4$ TeV. Hence, it is expected to achieve a lower statistical uncertainty of the cross section times branching ratio. For an exact estimation of the statistical uncertainty at this centre-of-mass energy, however, a dedicated study of all background processes at $\sqrt{s} = 3$ TeV has to be carried out.

8. Conclusion

The physics potential for the cross section times branching ratio $\sigma_{e^+e^-\to H\nu_e\bar{\nu}_e} \times BR_{H\to Z\gamma}$ measurement was estimated for a SM Higgs boson with a mass of $M_H = 126$ GeV produced in e^+e^- collisions at the CLIC collider at a centre-of-mass energy of $\sqrt{s} = 1.4$ TeV. The results are based on full CLIC_SiD_CDR detector simulations of e^+e^- collisions at CLIC using unpolarised beams and an integrated luminosity of $1.5\,ab^{-1}$. All relevant background processes, in particular $e^\pm\gamma$ collisions as well as beam-induced backgrounds from $\gamma\gamma \to$ hadrons processes are included.
Background processes from the e^+e^- initial state which produce exactly the same final state particles as the signal channel represent the dominant background processes for this study. In addition, processes with the initial state $e^\pm\gamma$ play a non-negligible role for this rare Higgs decay.
The combined statistical uncertainty of the cross section times branching ratio $\delta(\sigma \times BR_{H\to Z\gamma})$ has a value of approximately 42%. A potential improvement of the jet energy resolution currently under study for detectors at CLIC could result in a significant improvement of the analysis results. An optimisation of the photon and electron reconstruction and identification would lead, in this analysis, to a rather minor improvement of the statistical uncertainty of the cross section times branching ratio of a few percent. For a CLIC collider at $\sqrt{s} = 1.4$ TeV with -80% (left-handed) electron beam polarisation, the uncertainty can be reduced to approximately 31%.

A. Event properties used in the signal and background event classification

In the following Figures 9–37, the reconstructed event properties of signal and background events of the $H \to Z\gamma$ study after the two discussed selection steps are compared to each other. In the left panels (a,c,e), events after pre-selection cuts (cf. Section 5.1) are shown. In the right panels (b,d,f), events after the selection based on boosted decision trees (cf. Section 5.2) are shown. The reconstructed event properties are shown separately for the three studied signal channels $H \to Z\gamma; Z \to q\bar{q}$, $H \to Z\gamma; Z \to e^+e^-$ and $H \to Z\gamma; Z \to \mu^+\mu^-$.
The event properties are displayed in stacked histograms. The first entries at the bottom of each stacked histogram are the events of the signal events. Then, the background events separated per channel are added on top of the stack. Here, the background channel with the fewest events after pre-selection cuts is added to the histograms first and the one with the most events last. The *y*-axis of the histograms are displayed in logarithmic mode. This ensures that the contributions of all channels can be seen equally well, even if the number of events per channel differs in magnitude. For the comparison of events after the two discussed selection steps, the order of background channels in the histogram with events after the BDT-selection is chosen to be of the same order as chosen in the histogram of the events after pre-selection cuts.

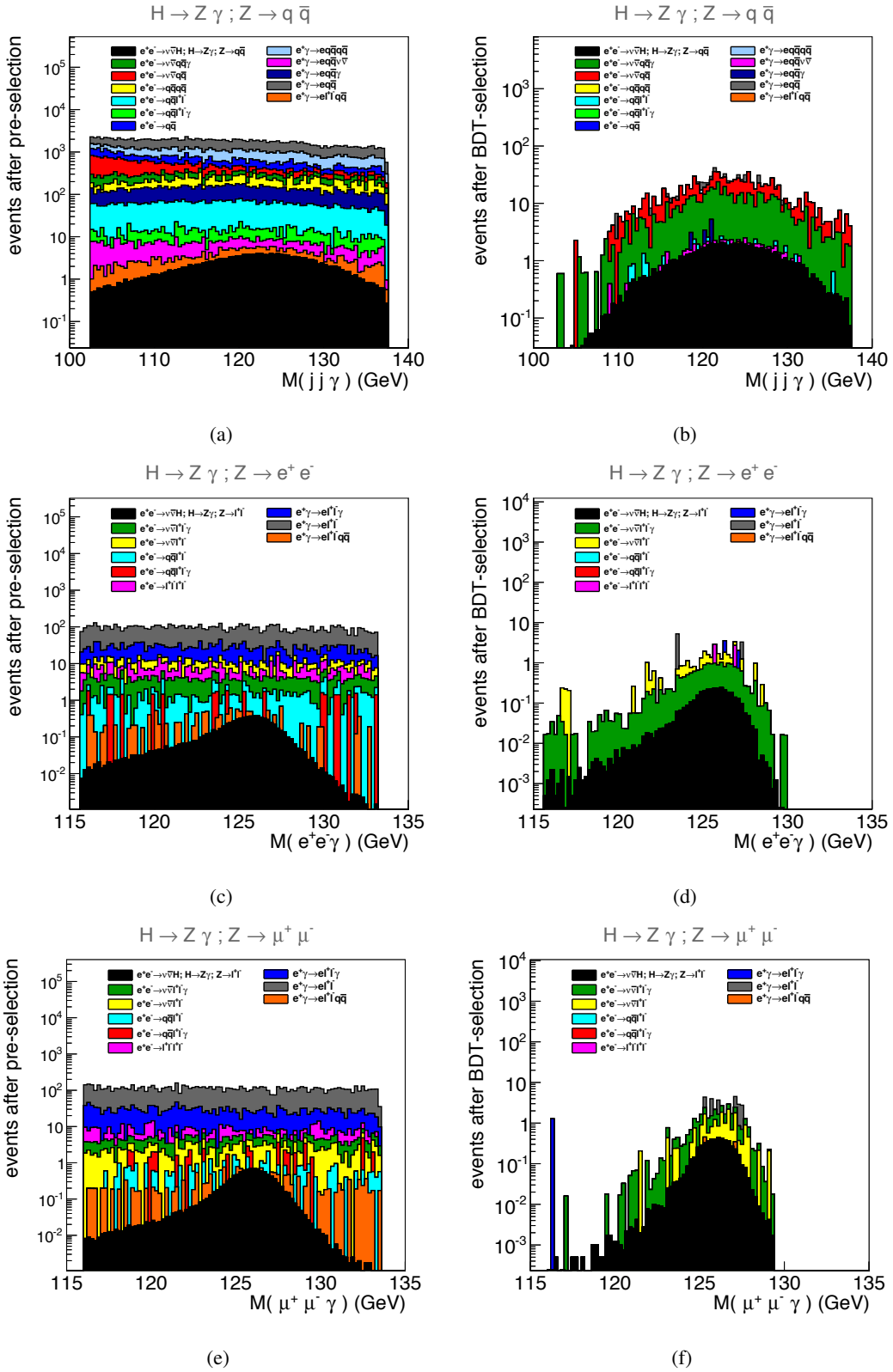

Figure 9: Invariant mass of H candidates in signal and background events for the $H \to Z\gamma; Z \to q\bar{q}$ channel (a,b), the $H \to Z\gamma; Z \to e^+e^-$ channel (c,d), and the $H \to Z\gamma; Z \to \mu^+\mu^-$ channel (e,f) after pre-selection (a,c,e) and after BDT-selection (b,d,f).

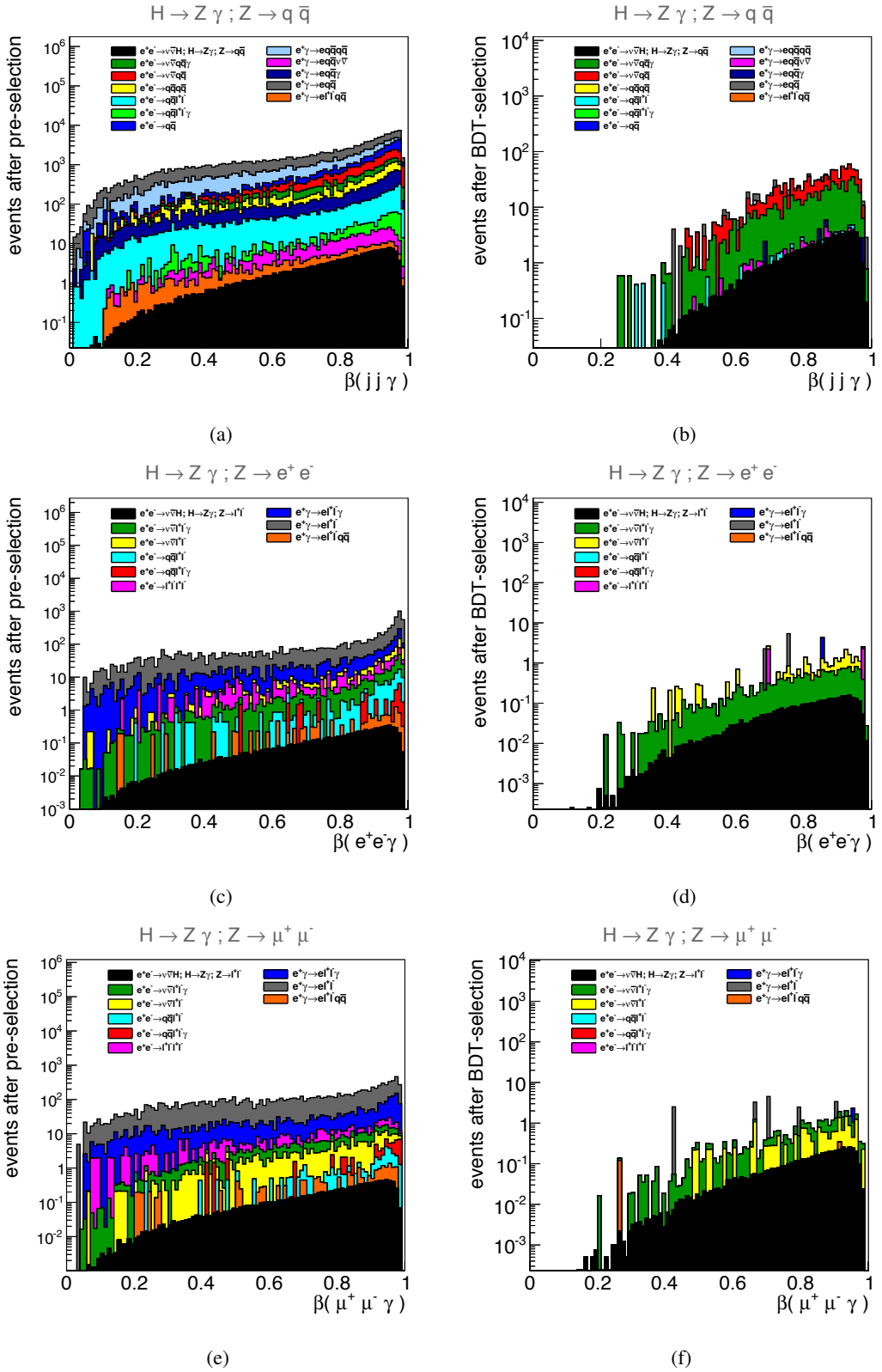

Figure 10: Velocity of H candidates in signal and background events for the $H \to Z\gamma; Z \to q\bar{q}$ channel (a,b), the $H \to Z\gamma; Z \to e^+e^-$ channel (c,d), and the $H \to Z\gamma; Z \to \mu^+\mu^-$ channel (e,f) after pre-selection (a,c,e) and after BDT-selection (b,d,f).

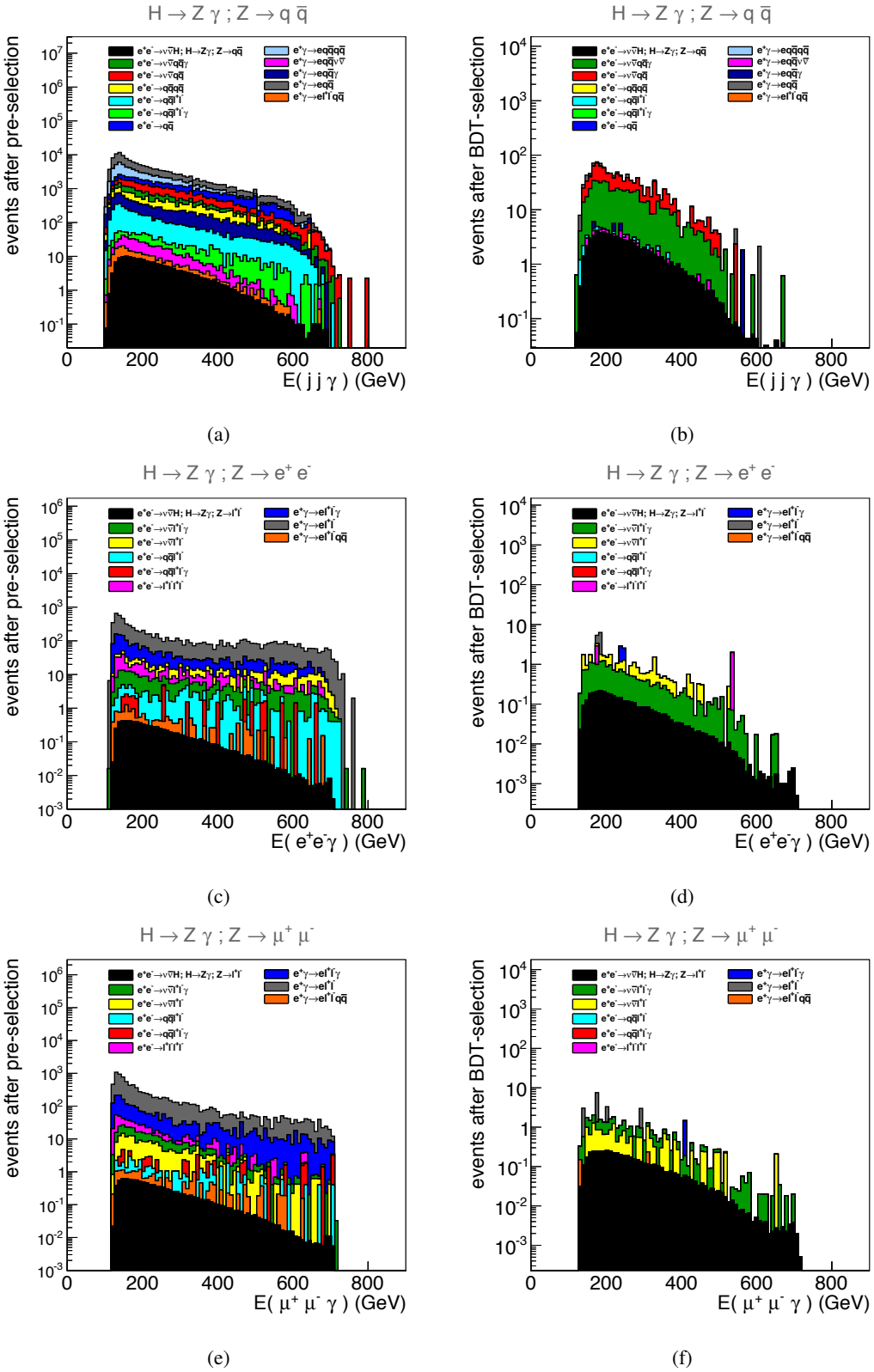

Figure 11: Energy of H candidates in signal and background events for the $H \to Z\gamma; Z \to q\bar{q}$ channel (a,b), the $H \to Z\gamma; Z \to e^+e^-$ channel (c,d), and the $H \to Z\gamma; Z \to \mu^+\mu^-$ channel (e,f) after pre-selection (a,c,e) and after BDT-selection (b,d,f).

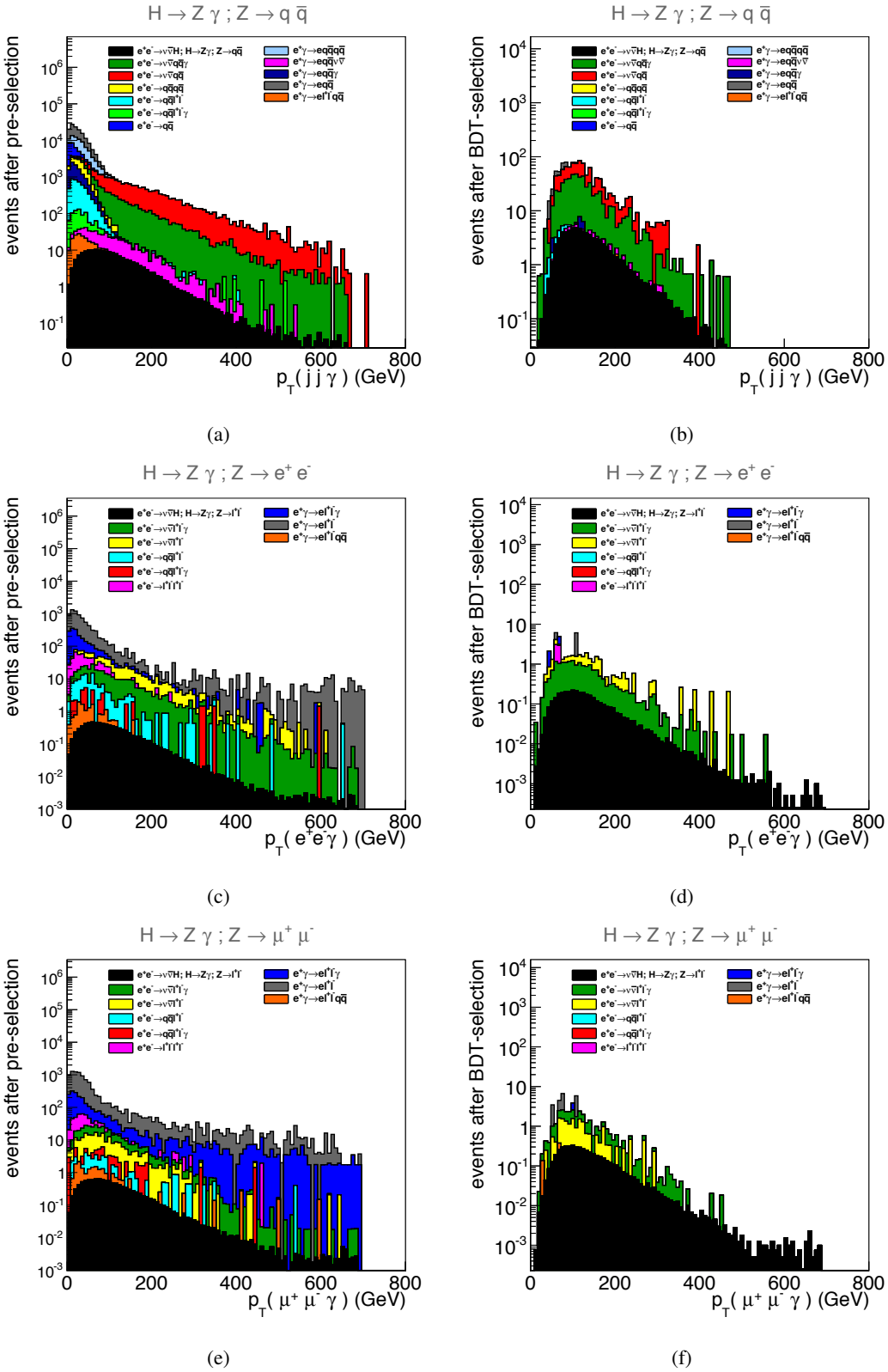

Figure 12: Transverse momentum of H candidates in signal and background events for the $H \to Z\gamma; Z \to q\bar{q}$ channel (a,b), the $H \to Z\gamma; Z \to e^+e^-$ channel (c,d), and the $H \to Z\gamma; Z \to \mu^+\mu^-$ channel (e,f) after pre-selection (a,c,e) and after BDT-selection (b,d,f).

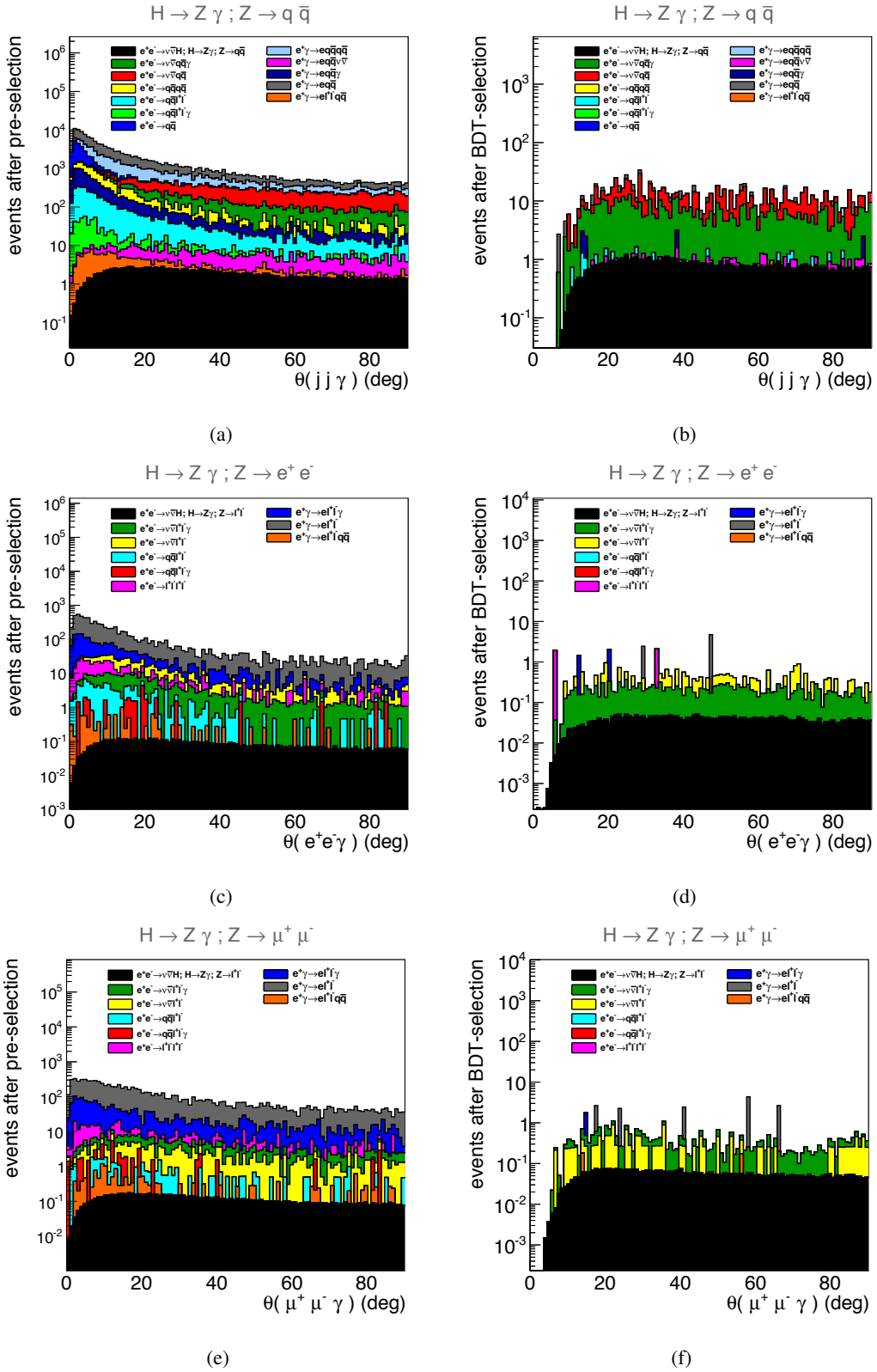

Figure 13: Polar angle of H candidates in signal and background events for the $H \to Z\gamma; Z \to q\bar{q}$ channel (a,b), the $H \to Z\gamma; Z \to e^+e^-$ channel (c,d), and the $H \to Z\gamma; Z \to \mu^+\mu^-$ channel (e,f) after pre-selection (a,c,e) and after BDT-selection (b,d,f).

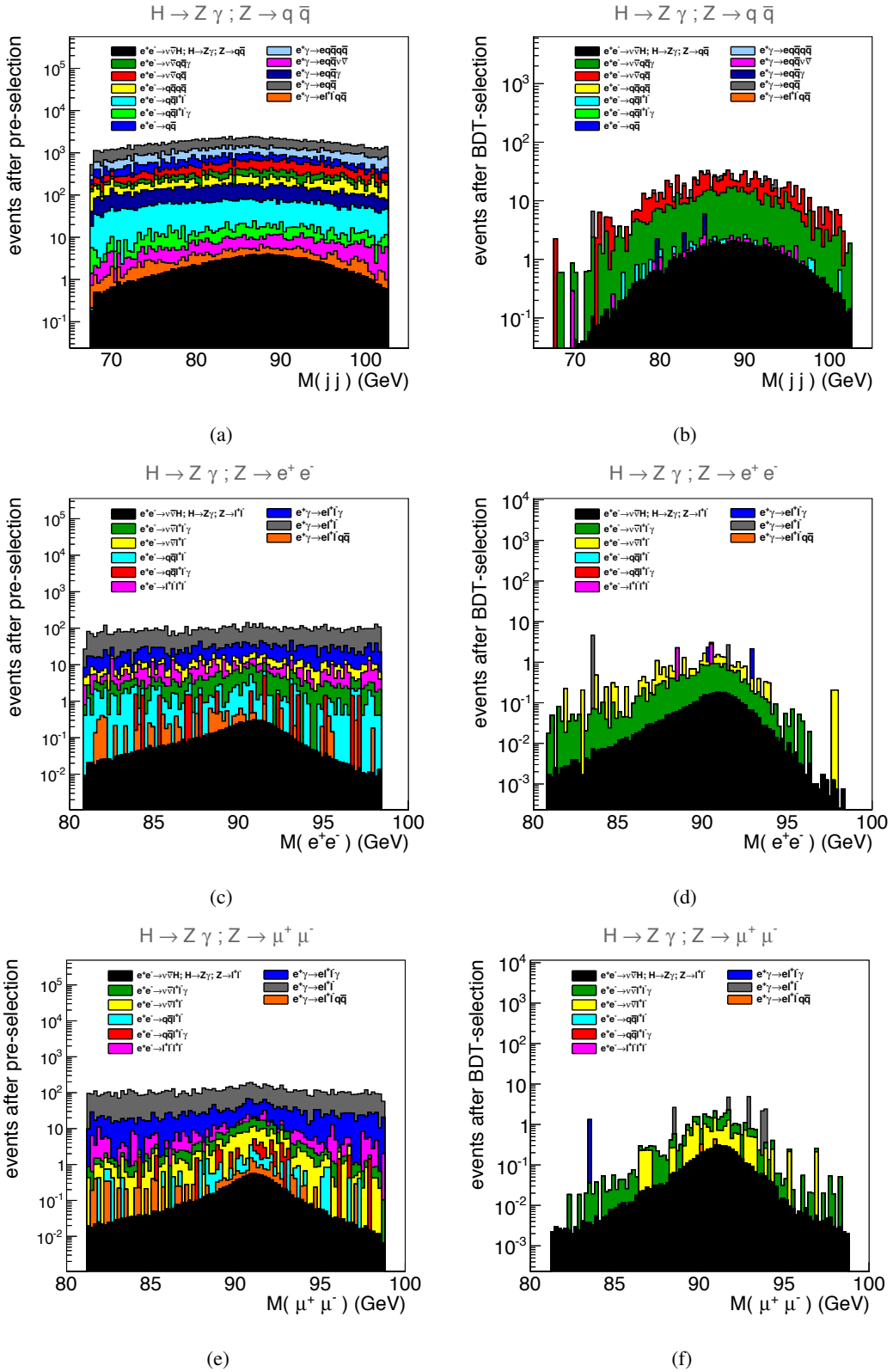

Figure 14: Invariant mass of Z candidates in signal and background events for the $H \to Z\gamma; Z \to q\bar{q}$ channel (a,b), the $H \to Z\gamma; Z \to e^+e^-$ channel (c,d), and the $H \to Z\gamma; Z \to \mu^+\mu^-$ channel (e,f) after pre-selection (a,c,e) and after BDT-selection (b,d,f).

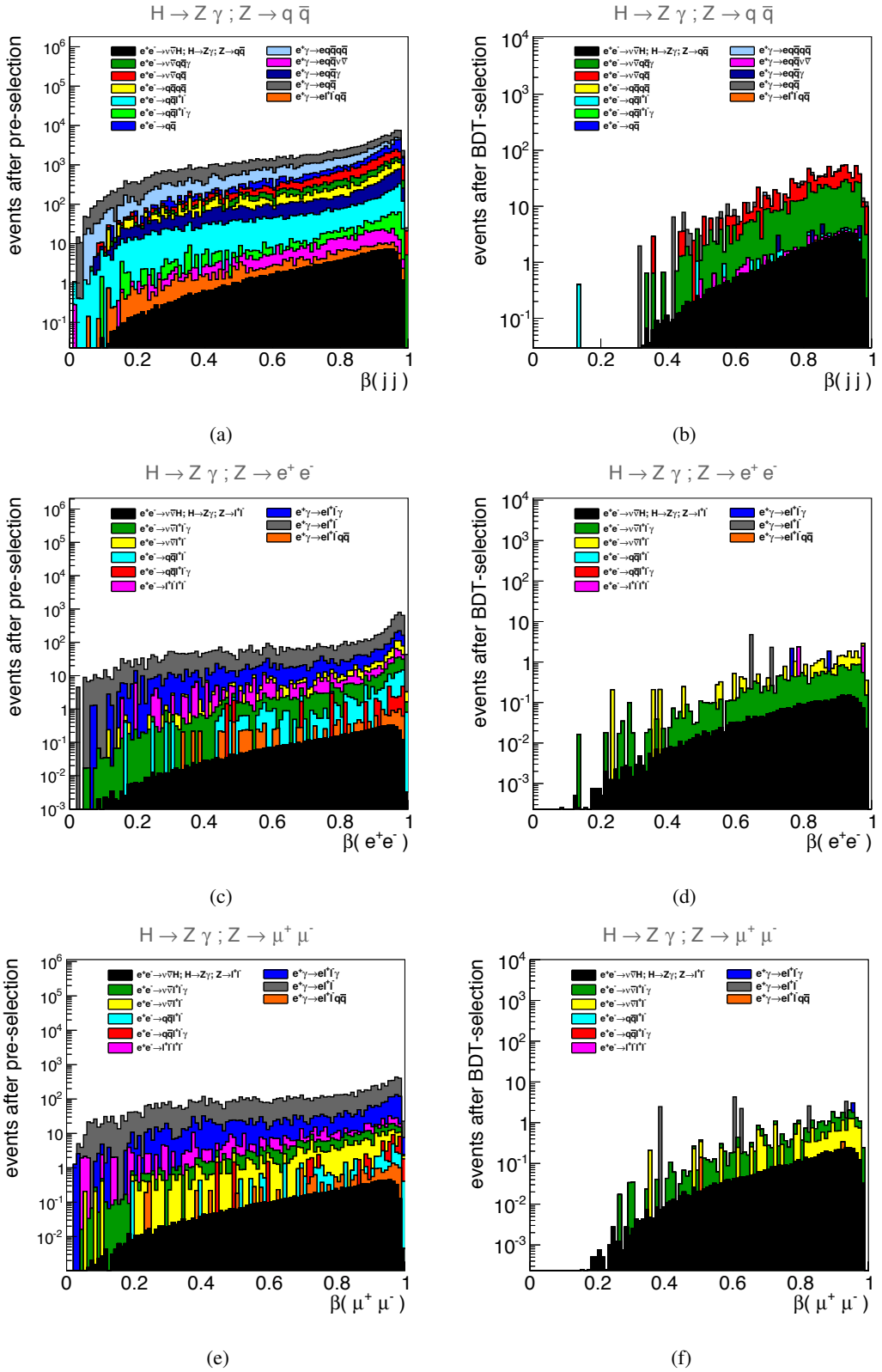

Figure 15: Velocity of Z candidates in signal and background events for the $H \to Z\gamma; Z \to q\bar{q}$ channel (a,b), the $H \to Z\gamma; Z \to e^+e^-$ channel (c,d), and the $H \to Z\gamma; Z \to \mu^+\mu^-$ channel (e,f) after pre-selection (a,c,e) and after BDT-selection (b,d,f).

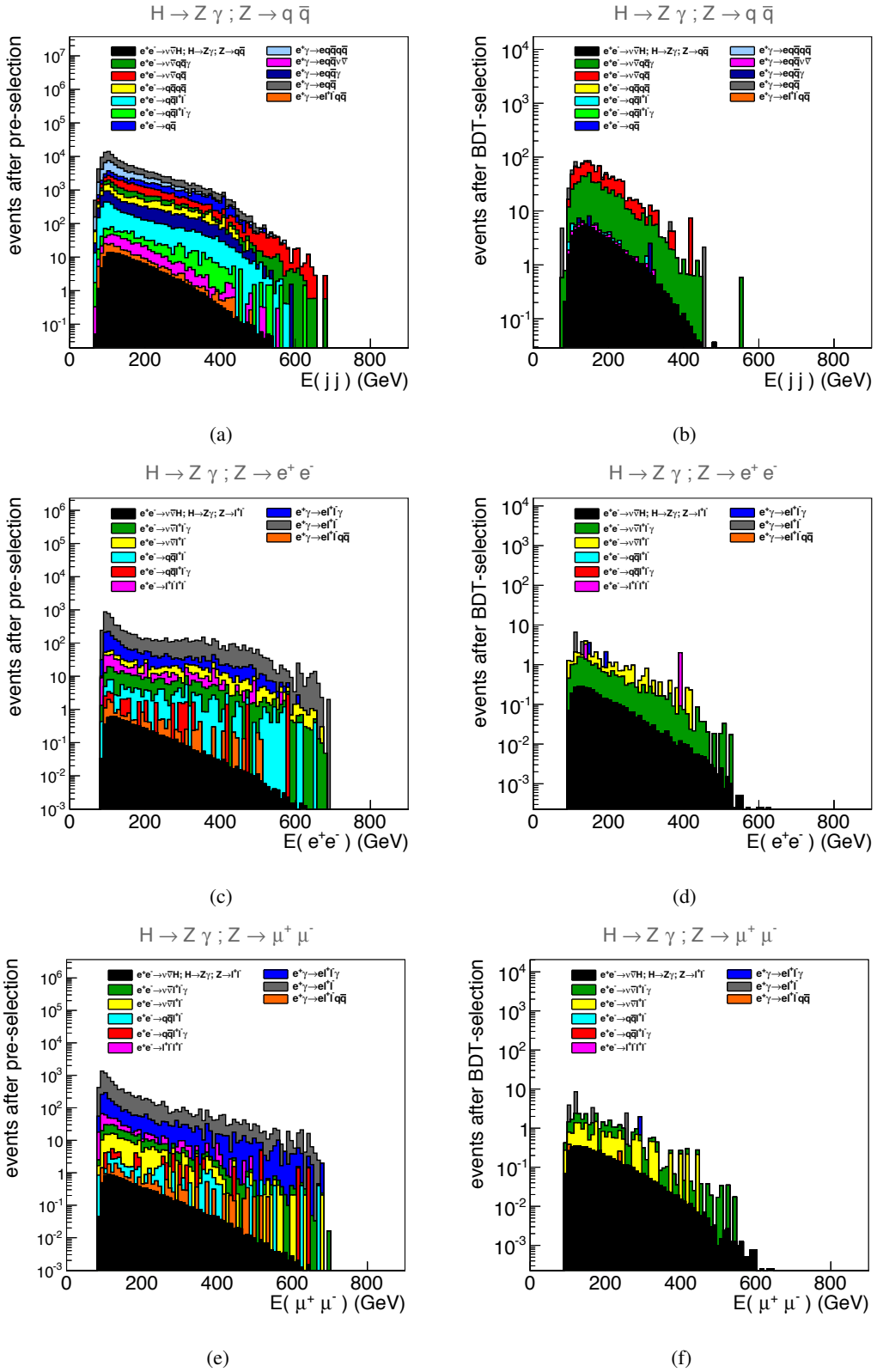

Figure 16: Energy of Z candidates in signal and background events for the $H \to Z\gamma; Z \to q\bar{q}$ channel (a,b), the $H \to Z\gamma; Z \to e^+e^-$ channel (c,d), and the $H \to Z\gamma; Z \to \mu^+\mu^-$ channel (e,f) after pre-selection (a,c,e) and after BDT-selection (b,d,f).

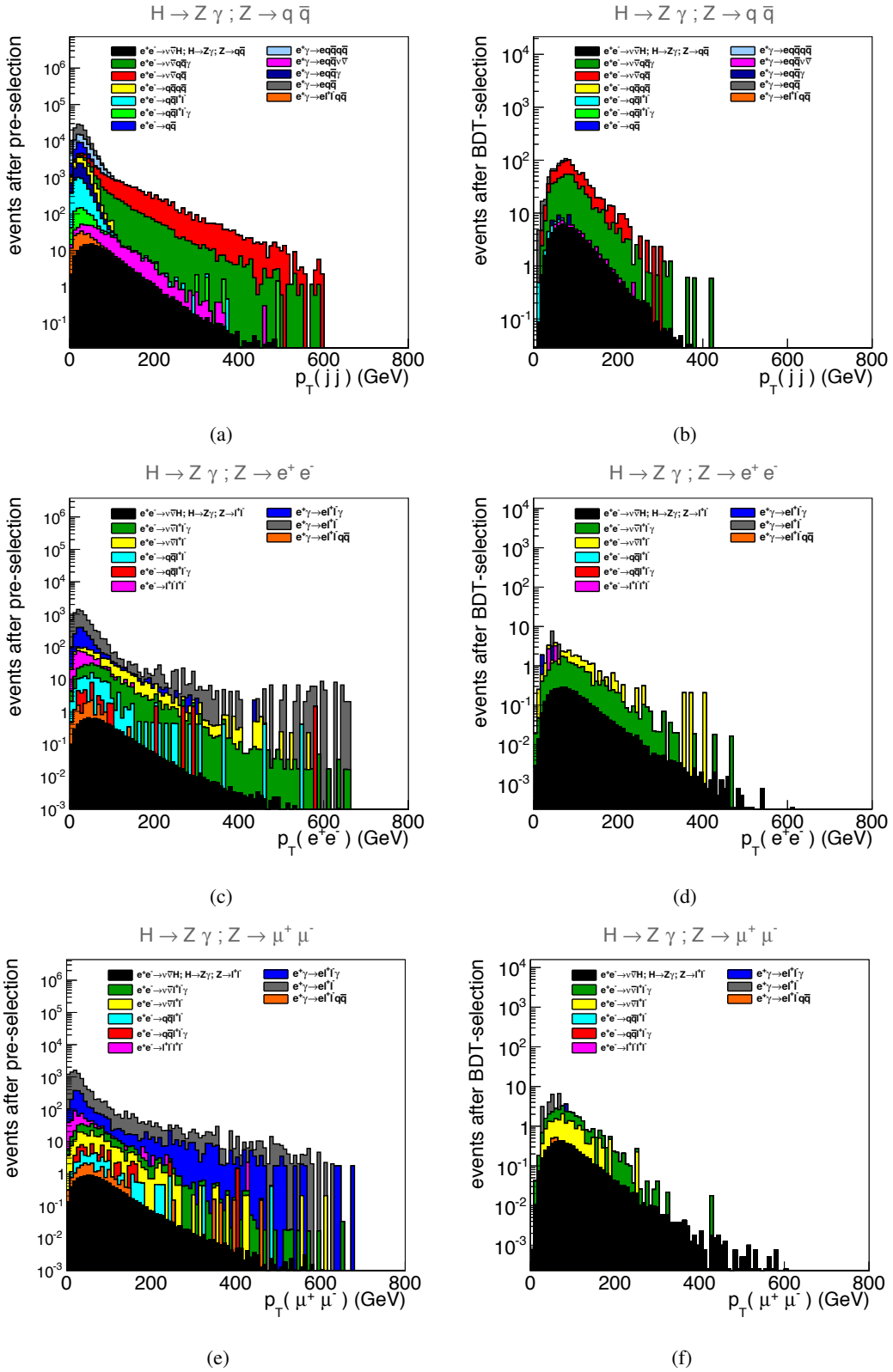

Figure 17: Transverse momentum of Z candidates in signal and background events for the $H \to Z\gamma; Z \to q\bar{q}$ channel (a,b), the $H \to Z\gamma; Z \to e^+e^-$ channel (c,d), and the $H \to Z\gamma; Z \to \mu^+\mu^-$ channel (e,f) after pre-selection (a,c,e) and after BDT-selection (b,d,f).

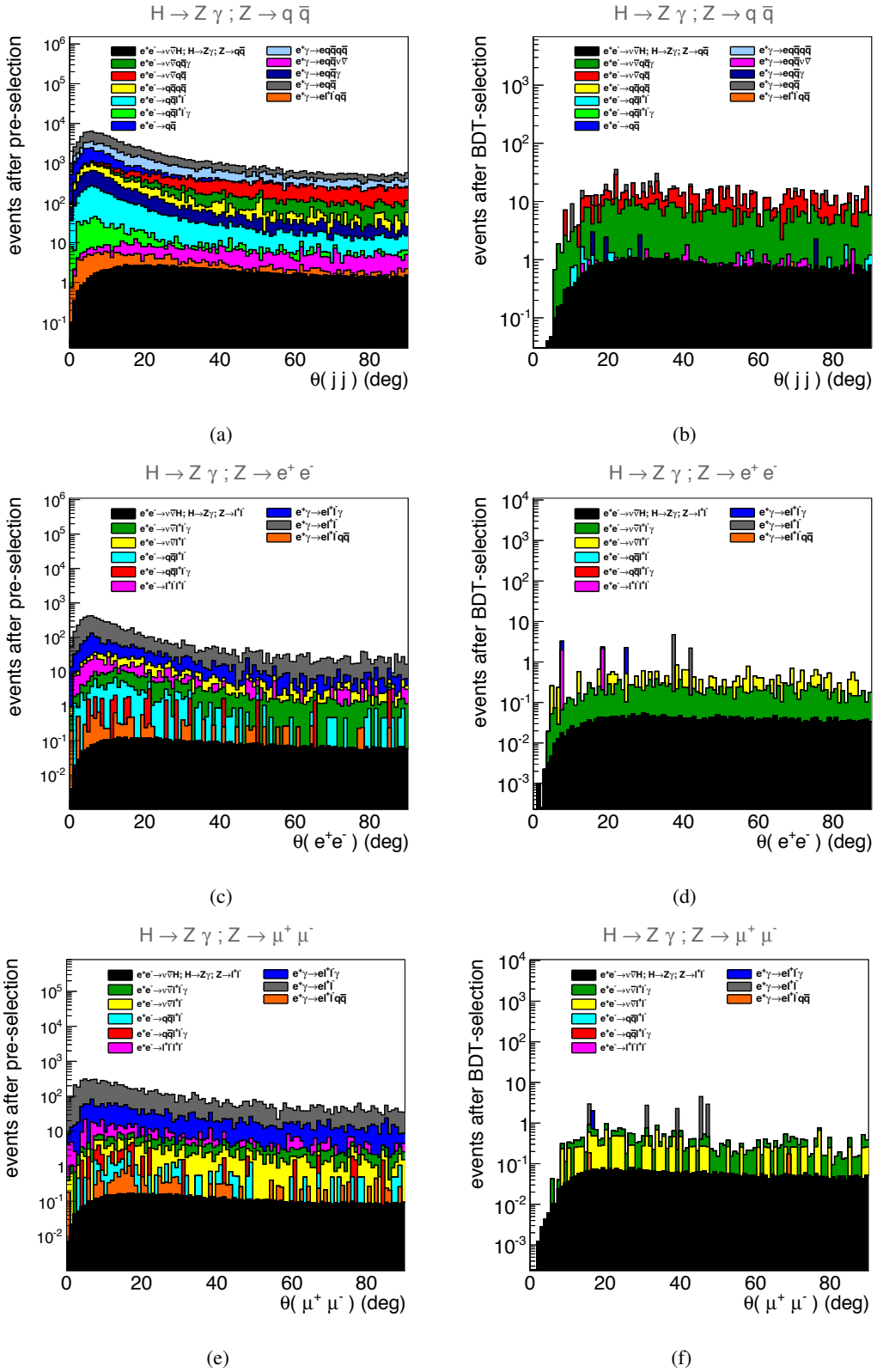

Figure 18: Polar angle of Z candidates in signal and background events for the $H \to Z\gamma; Z \to q\bar{q}$ channel (a,b), the $H \to Z\gamma; Z \to e^+e^-$ channel (c,d), and the $H \to Z\gamma; Z \to \mu^+\mu^-$ channel (e,f) after pre-selection (a,c,e) and after BDT-selection (b,d,f).

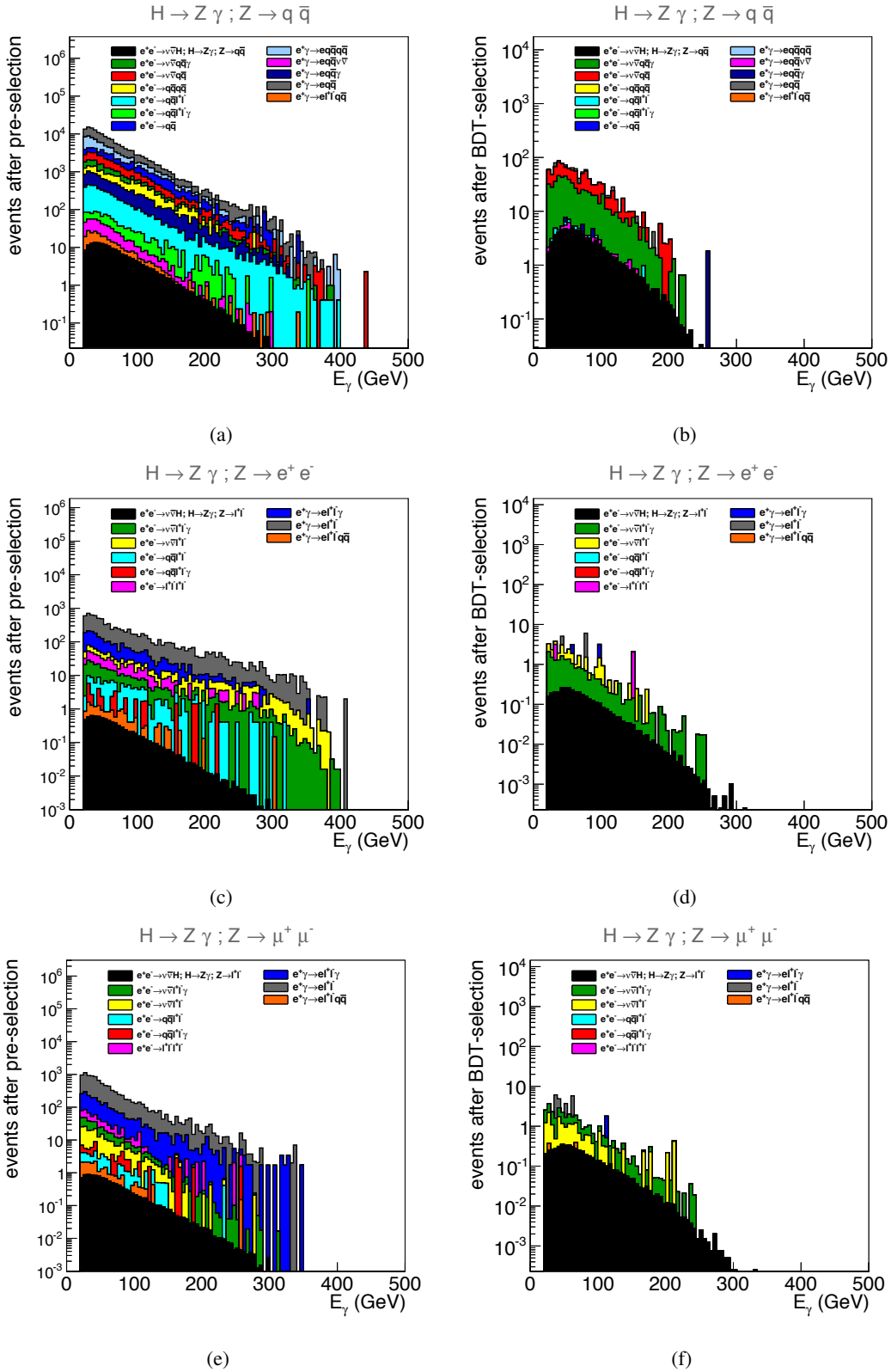

Figure 19: Energy of γ candidates in signal and background events for the $H \to Z\gamma; Z \to q\bar{q}$ channel (a,b), the $H \to Z\gamma; Z \to e^+e^-$ channel (c,d), and the $H \to Z\gamma; Z \to \mu^+\mu^-$ channel (e,f) after pre-selection (a,c,e) and after BDT-selection (b,d,f).

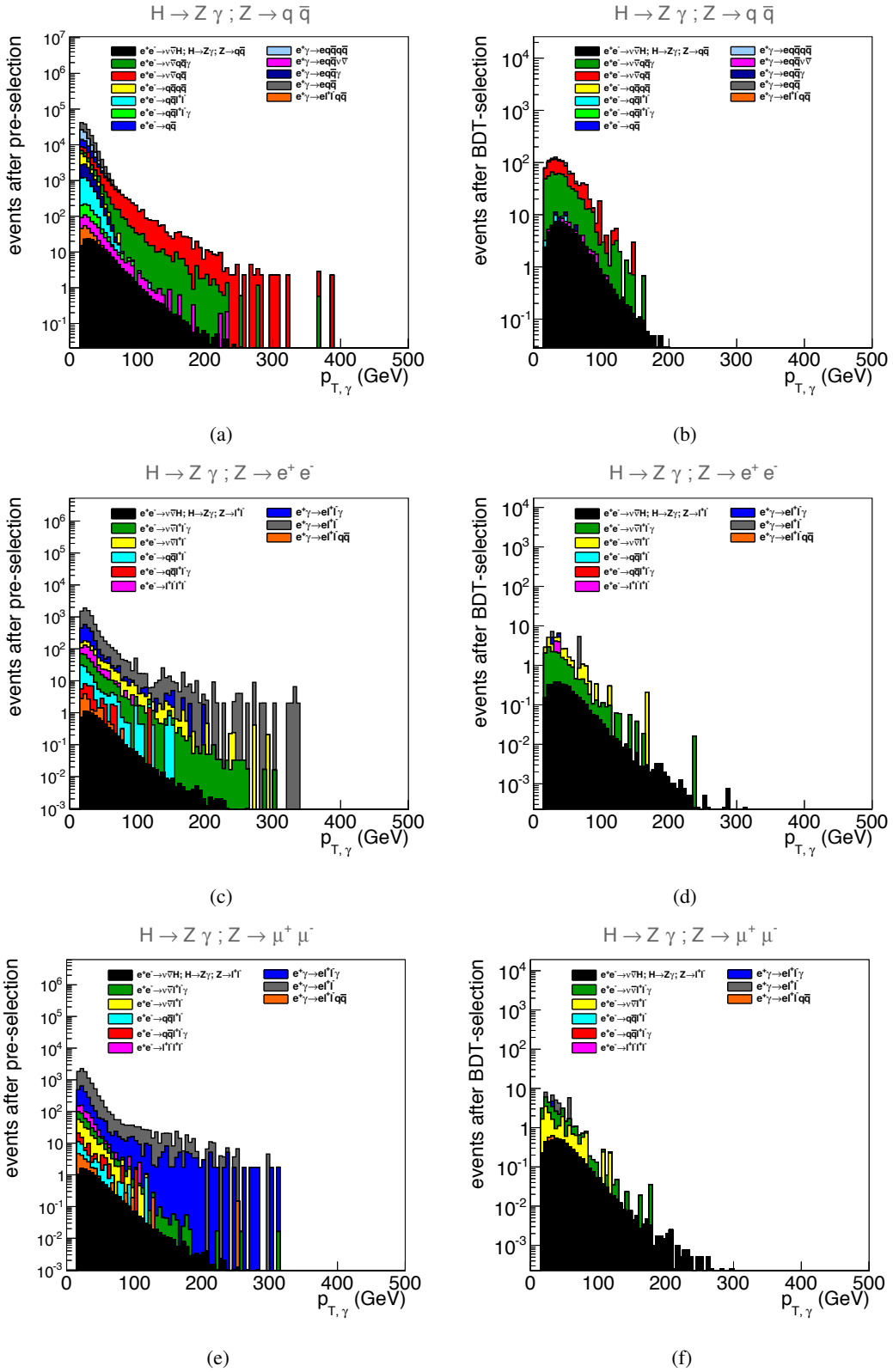

(a) (b) (c) (d) (e) (f)

Figure 20: Transverse momentum of γ candidates in signal and background events for the $H \to Z\gamma; Z \to q\bar{q}$ channel (a,b), the $H \to Z\gamma; Z \to e^+e^-$ channel (c,d), and the $H \to Z\gamma; Z \to \mu^+\mu^-$ channel (e,f) after pre-selection (a,c,e) and after BDT-selection (b,d,f).

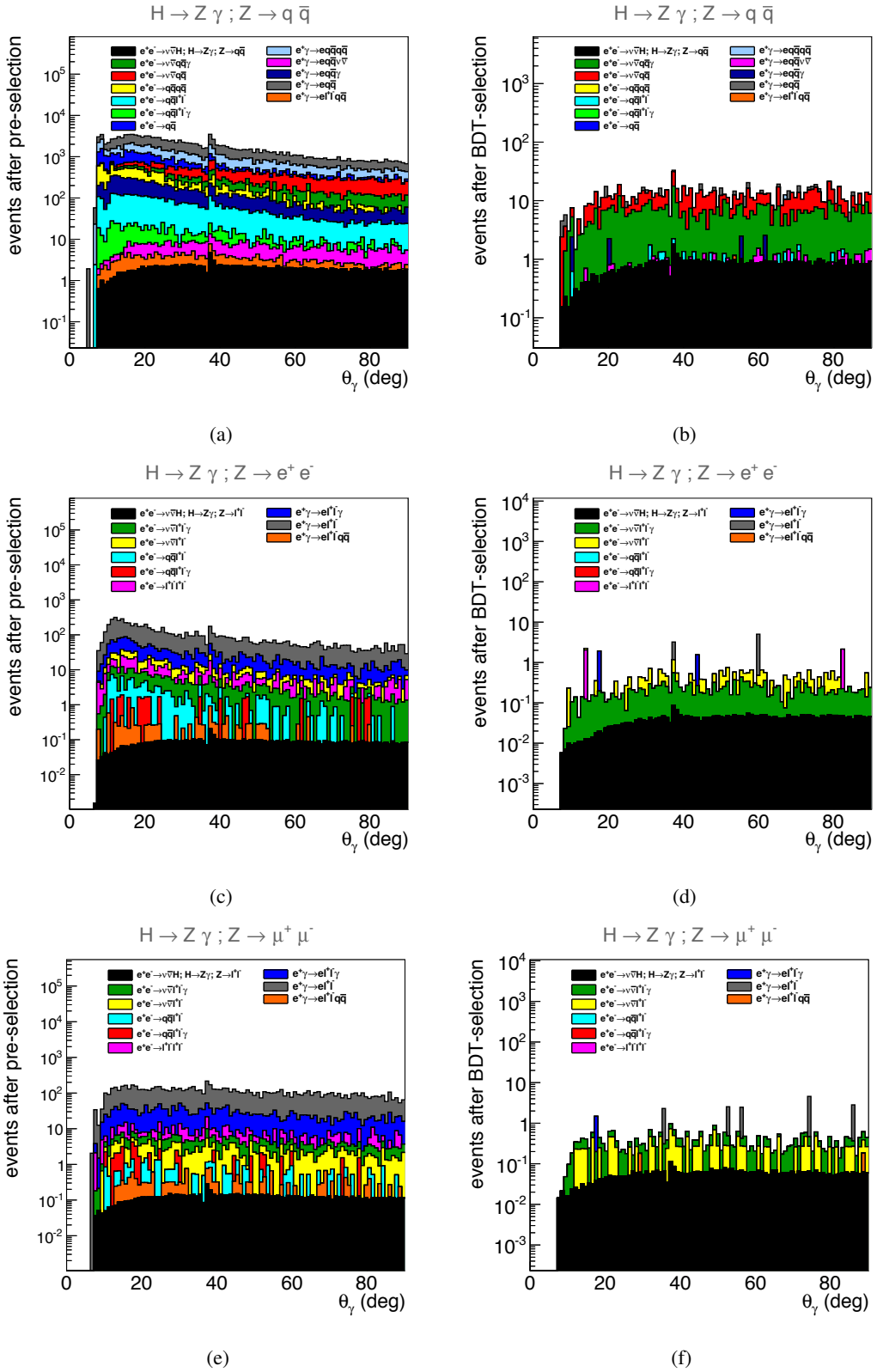

Figure 21: Polar angle of γ candidates in signal and background events for the $H \to Z\gamma; Z \to q\bar{q}$ channel (a,b), the $H \to Z\gamma; Z \to e^+e^-$ channel (c,d), and the $H \to Z\gamma; Z \to \mu^+\mu^-$ channel (e,f) after pre-selection (a,c,e) and after BDT-selection (b,d,f).

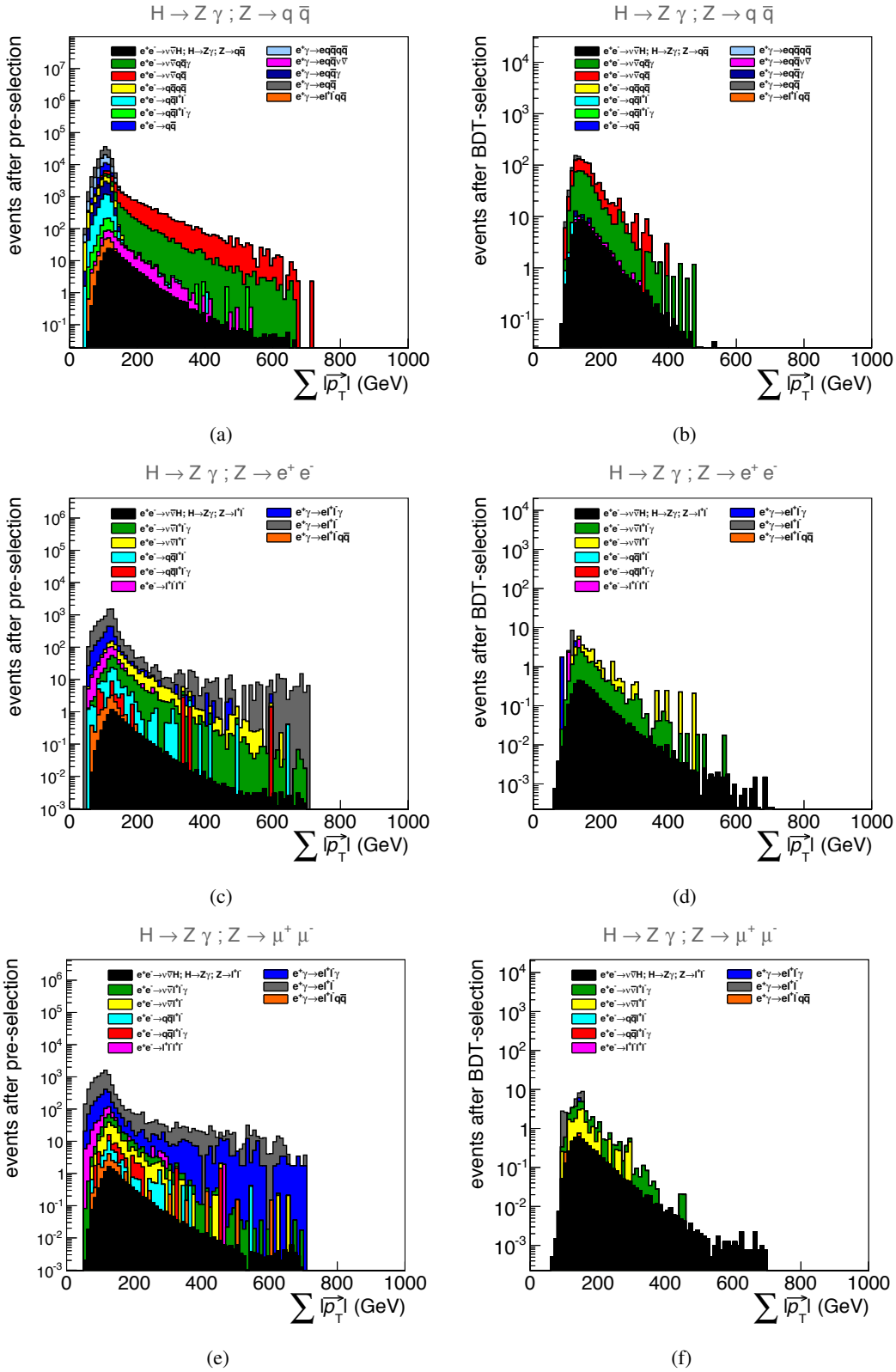

Figure 22: Scalar sum of transverse momenta of Z and γ in signal and background events for the $H \to Z\gamma; Z \to q\bar{q}$ channel (a,b), the $H \to Z\gamma; Z \to e^+e^-$ channel (c,d), and the $H \to Z\gamma; Z \to \mu^+\mu^-$ channel (e,f) after pre-selection (a,c,e) and after BDT-selection (b,d,f).

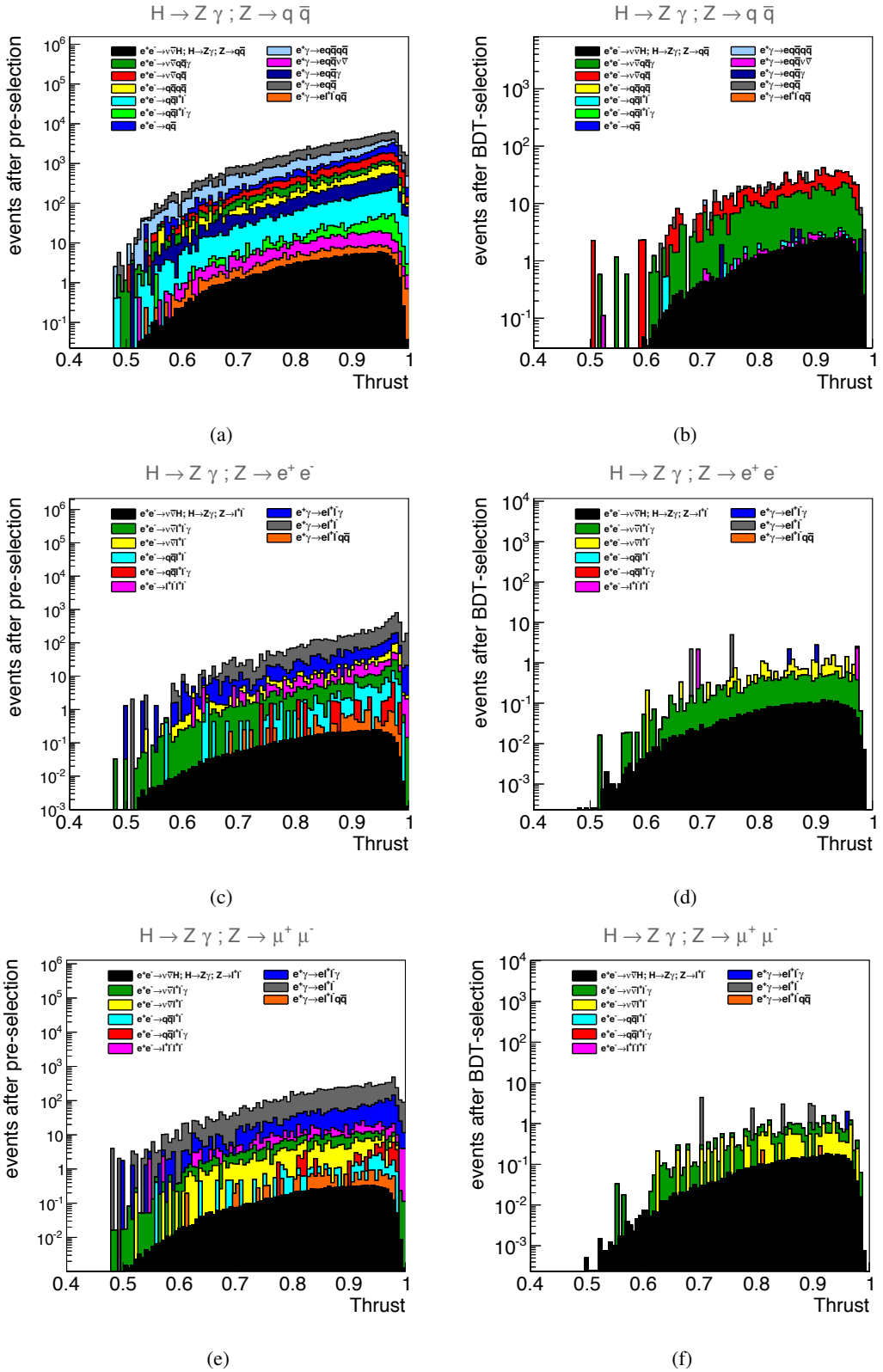

Figure 23: Thrust of signal and background events for the $H \to Z\gamma; Z \to q\bar{q}$ channel (a,b), the $H \to Z\gamma; Z \to e^+e^-$ channel (c,d), and the $H \to Z\gamma; Z \to \mu^+\mu^-$ channel (e,f) after pre-selection (a,c,e) and after BDT-selection (b,d,f).

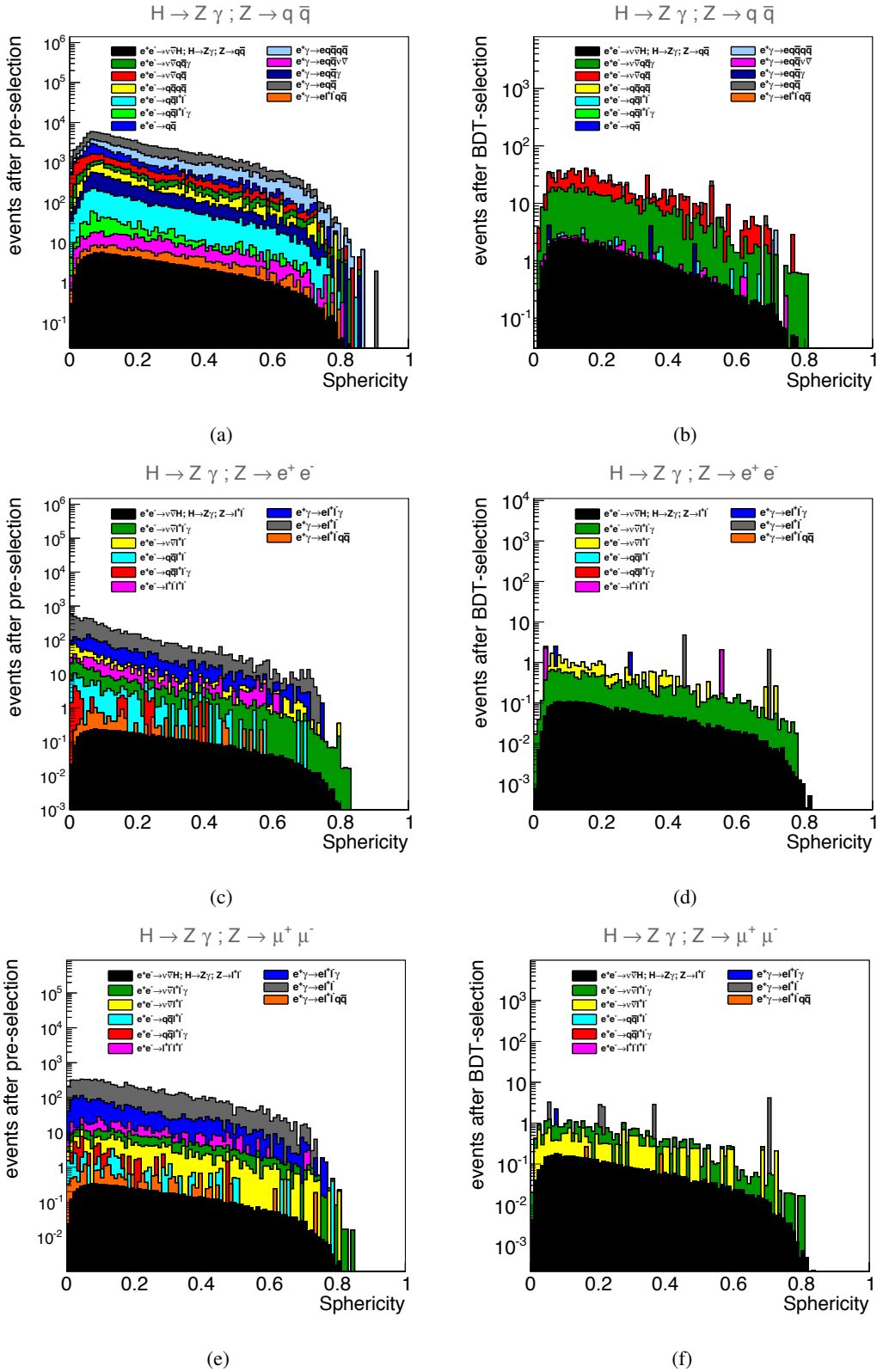

Figure 24: Sphericity of signal and background events for the $H \to Z\gamma; Z \to q\bar{q}$ channel (a,b), the $H \to Z\gamma; Z \to e^+e^-$ channel (c,d), and the $H \to Z\gamma; Z \to \mu^+\mu^-$ channel (e,f) after pre-selection (a,c,e) and after BDT-selection (b,d,f).

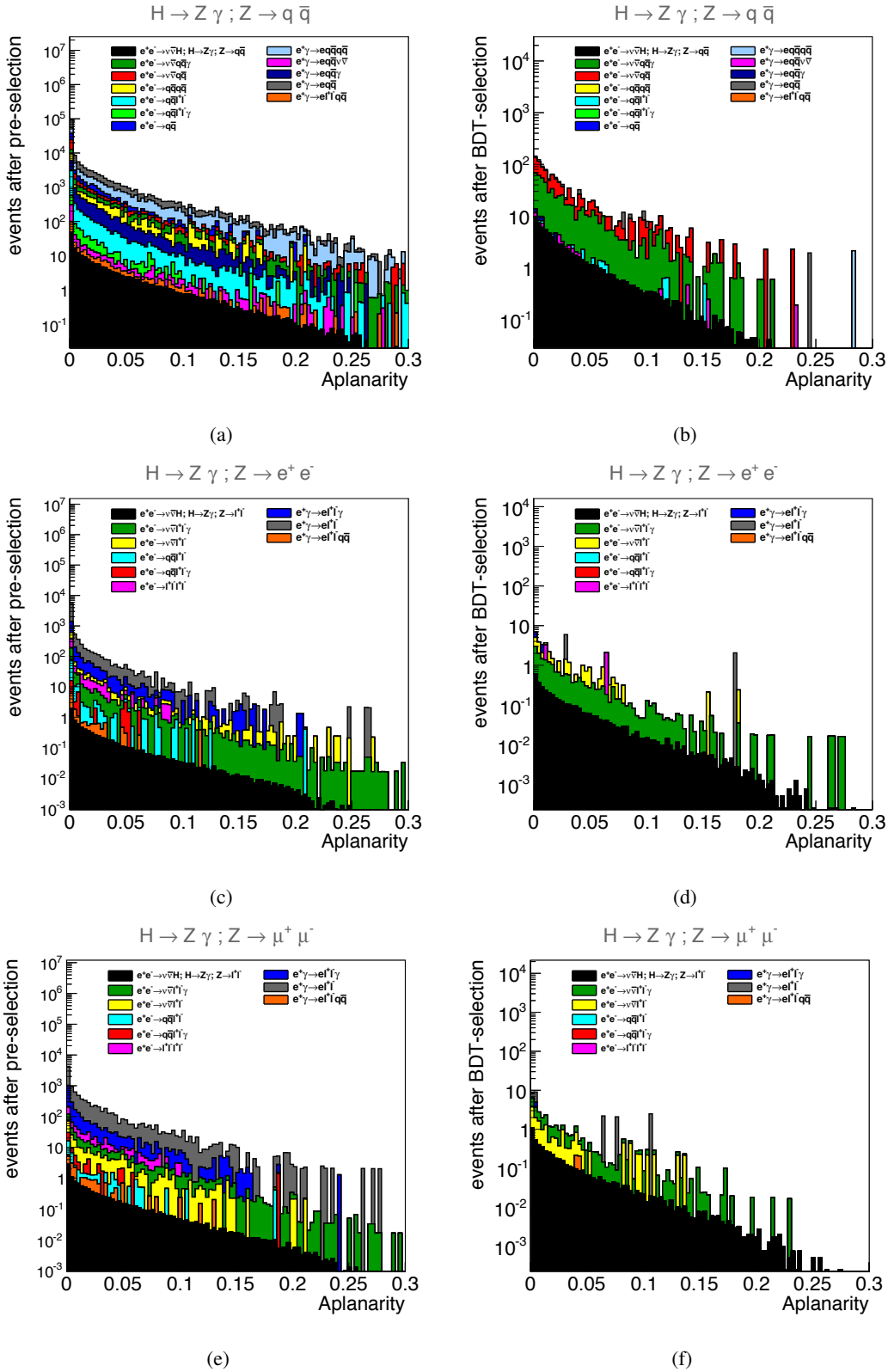

Figure 25: Aplanarity of signal and background events for the $H \to Z\gamma; Z \to q\bar{q}$ channel (a,b), the $H \to Z\gamma; Z \to e^+e^-$ channel (c,d), and the $H \to Z\gamma; Z \to \mu^+\mu^-$ channel (e,f) after pre-selection (a,c,e) and after BDT-selection (b,d,f).

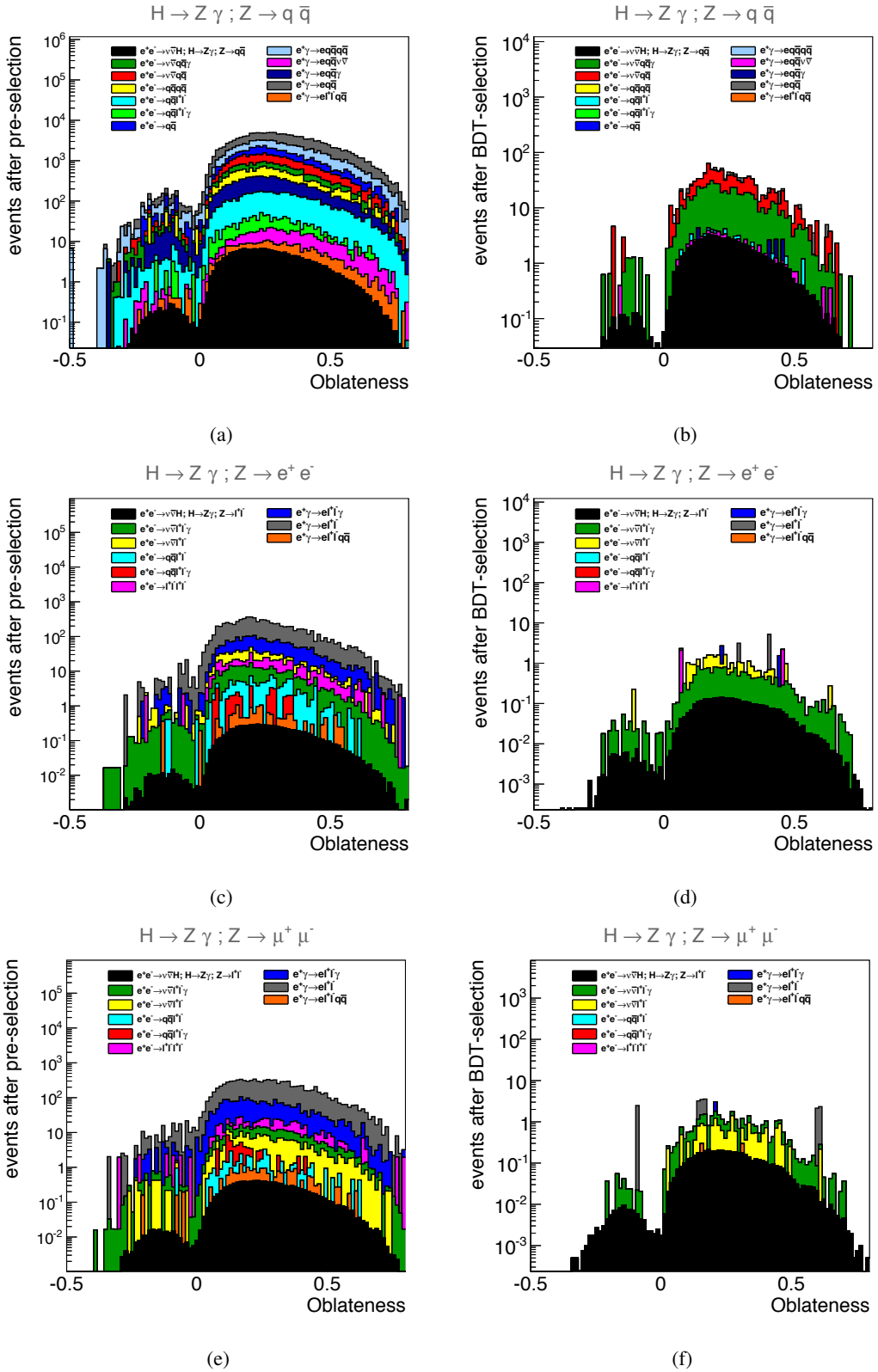

Figure 26: Oblateness of signal and background events for the $H \to Z\gamma; Z \to q\bar{q}$ channel (a,b), the $H \to Z\gamma; Z \to e^+e^-$ channel (c,d), and the $H \to Z\gamma; Z \to \mu^+\mu^-$ channel (e,f) after pre-selection (a,c,e) and after BDT-selection (b,d,f).

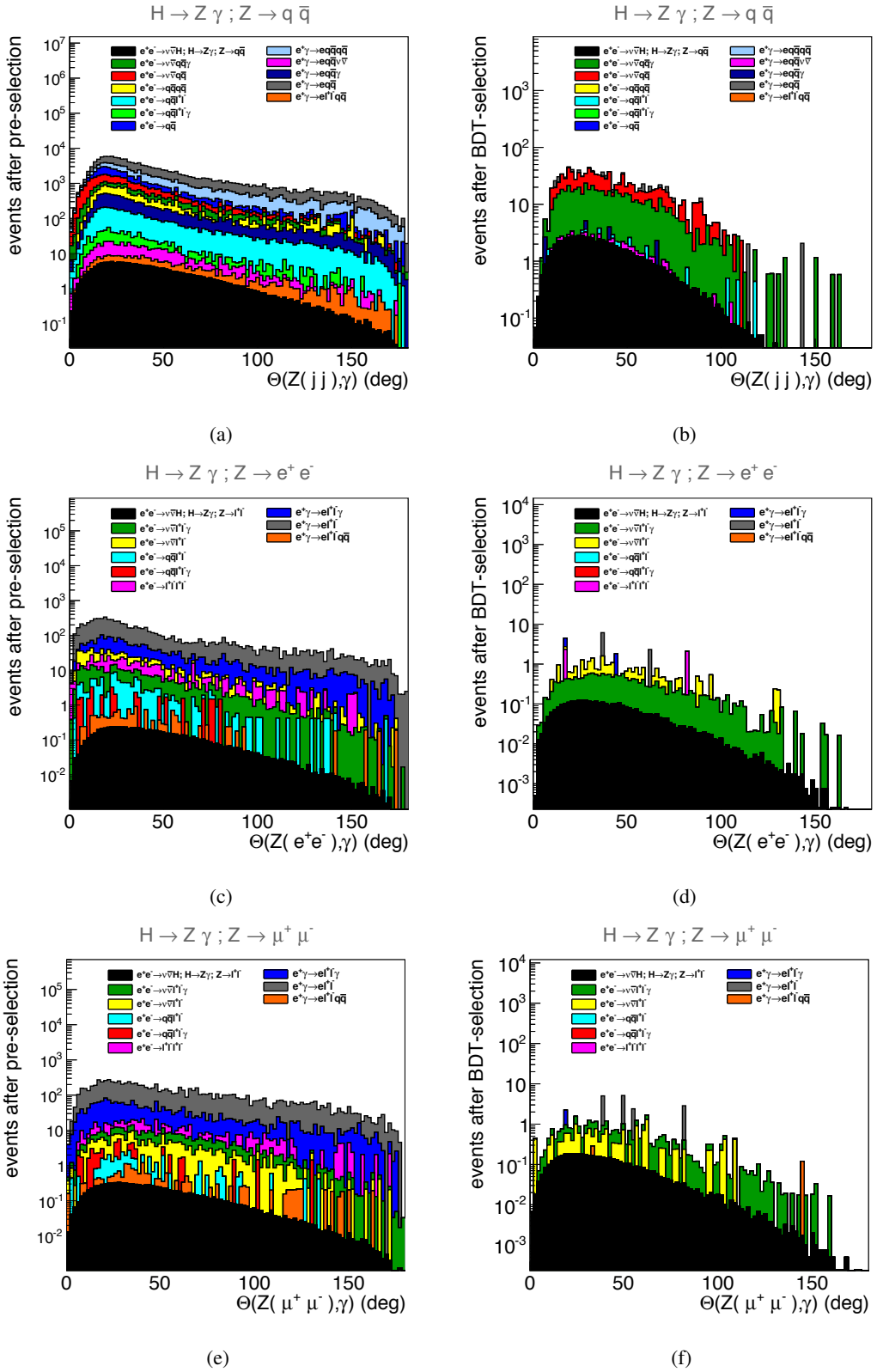

Figure 27: Angle between Z and γ of signal and background events for the $H \to Z\gamma; Z \to q\bar{q}$ channel (a,b), the $H \to Z\gamma; Z \to e^+e^-$ channel (c,d), and the $H \to Z\gamma; Z \to \mu^+\mu^-$ channel (e,f) after pre-selection (a,c,e) and after BDT-selection (b,d,f).

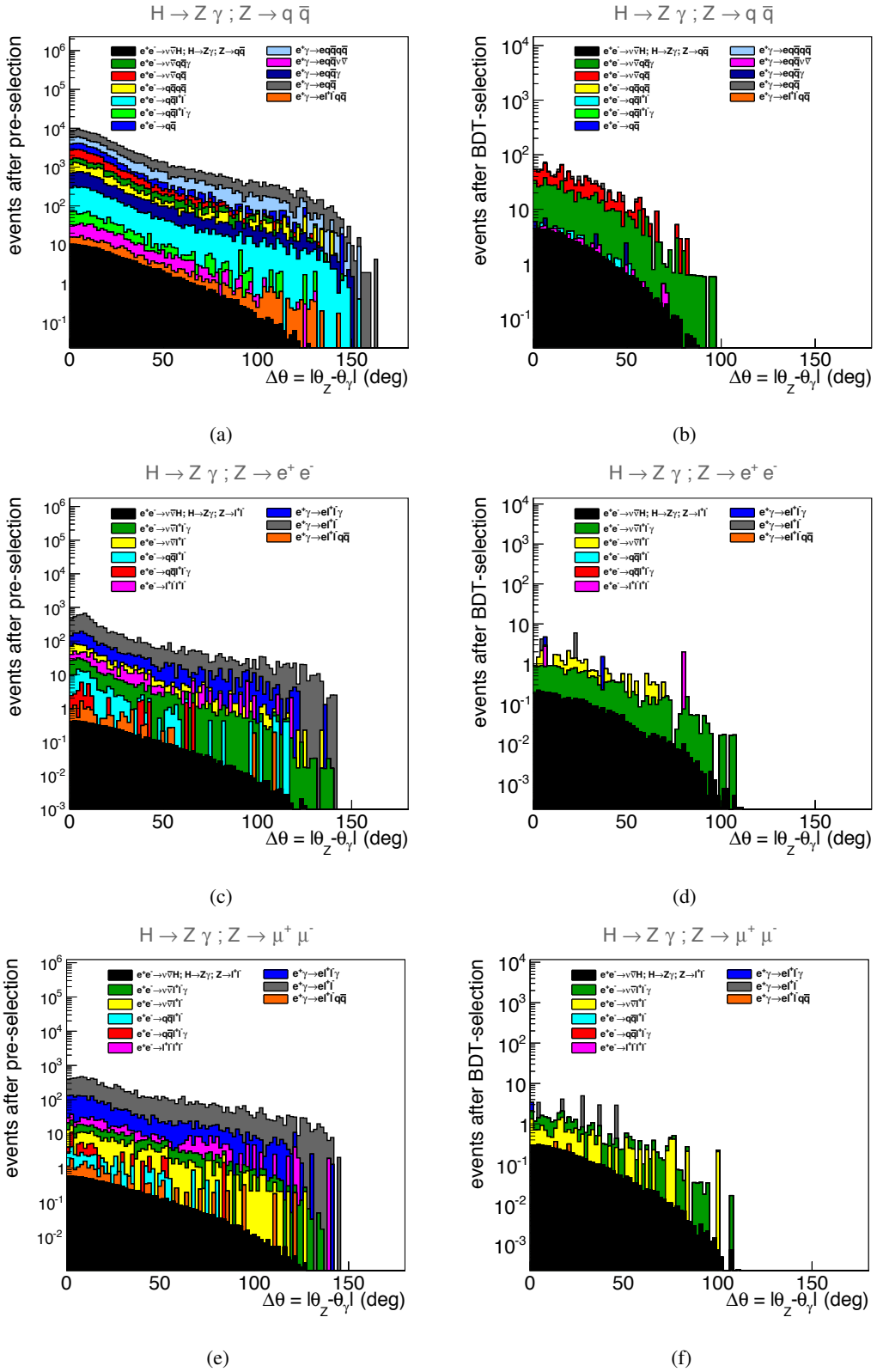

Figure 28: $\Delta\theta$ between Z and γ candidates of signal and background events for the $H \to Z\gamma; Z \to q\bar{q}$ channel (a,b), the $H \to Z\gamma; Z \to e^+e^-$ channel (c,d), and the $H \to Z\gamma; Z \to \mu^+\mu^-$ channel (e,f) after pre-selection (a,c,e) and after BDT-selection (b,d,f).

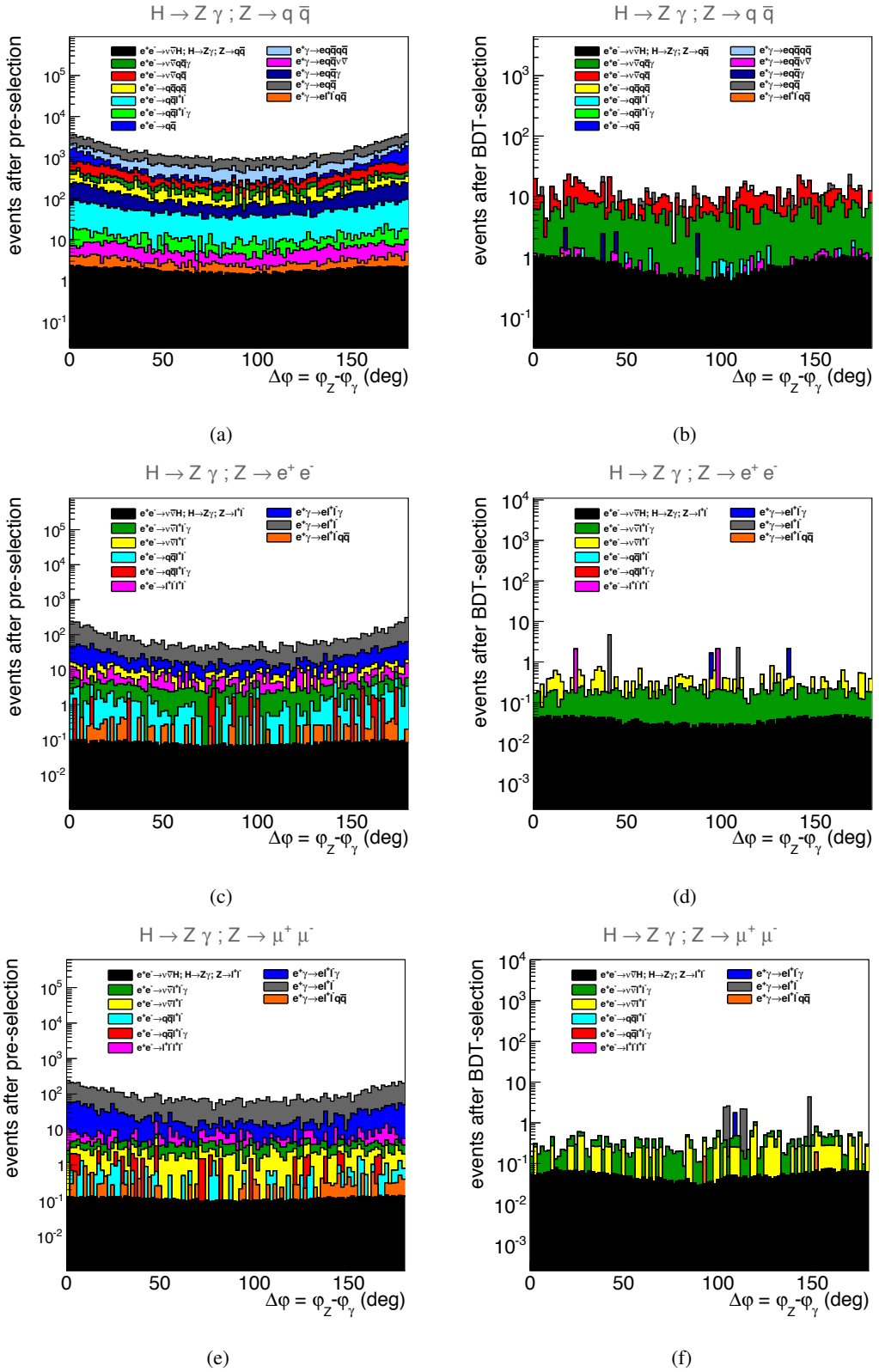

Figure 29: $\Delta\varphi$ between reconstructed Z and γ candidates of signal and background events for the $H \to Z\gamma; Z \to q\bar{q}$ channel (a,b), the $H \to Z\gamma; Z \to e^+e^-$ channel (c,d), and the $H \to Z\gamma; Z \to \mu^+\mu^-$ channel (e,f) after pre-selection (a,c,e) and after BDT-selection (b,d,f).

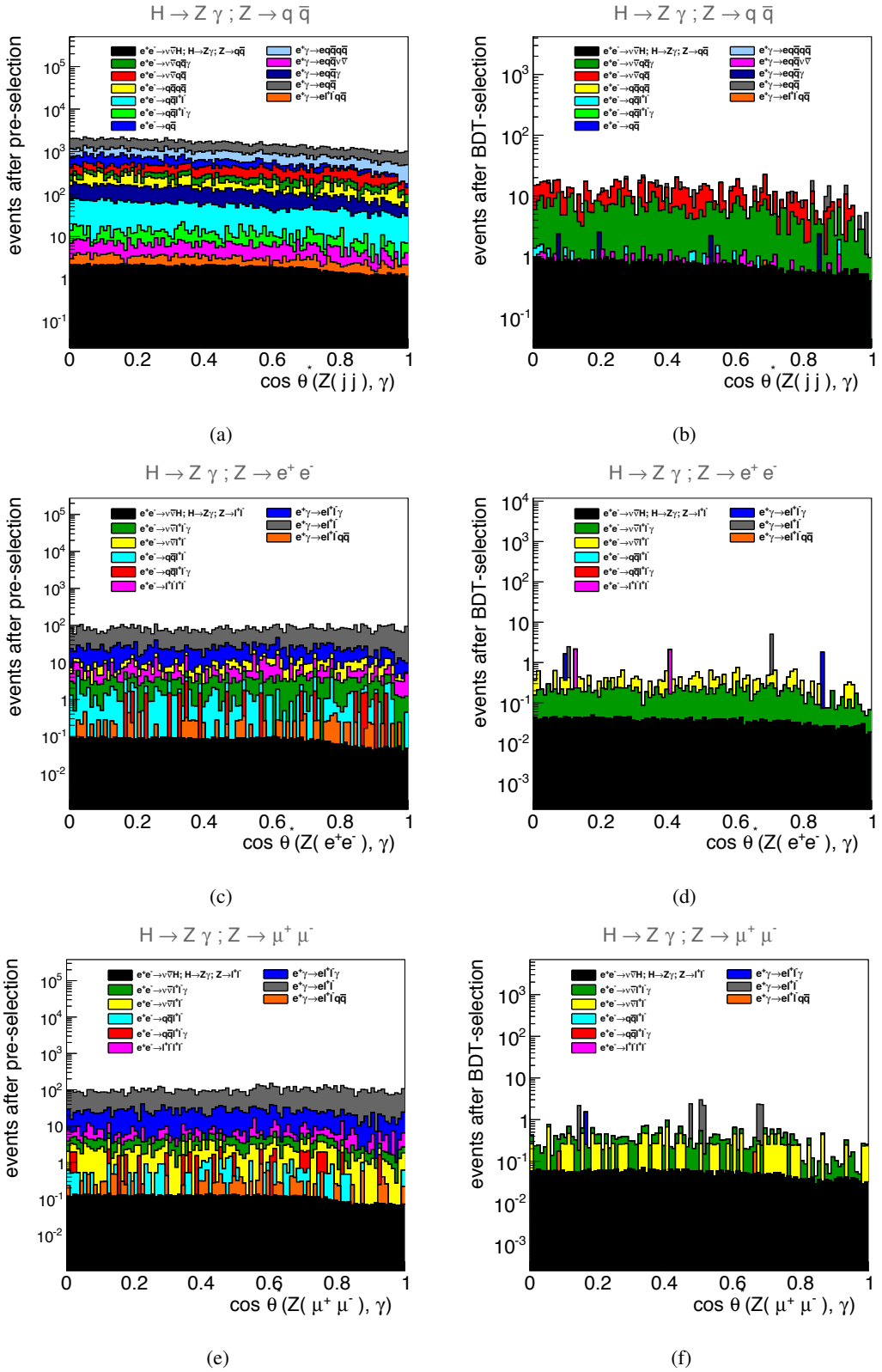

(a) (b) (c) (d) (e) (f)

Figure 30: Helicity angle between Z and γ candidates of signal and background events for the $H \to Z\gamma; Z \to q\bar{q}$ channel (a,b), the $H \to Z\gamma; Z \to e^+e^-$ channel (c,d), and the $H \to Z\gamma; Z \to \mu^+\mu^-$ channel (e,f) after pre-selection (a,c,e) and after BDT-selection (b,d,f).

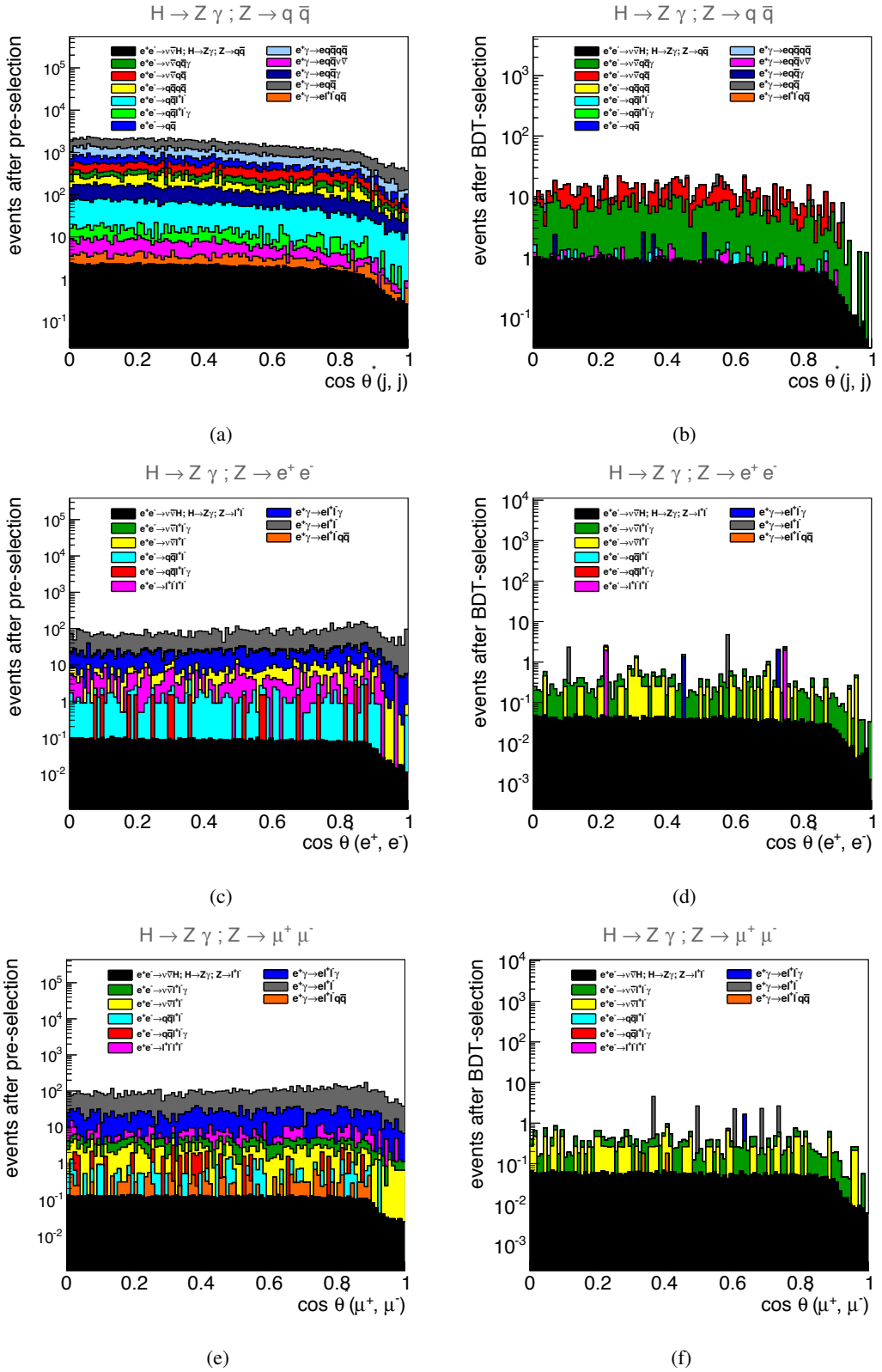

Figure 31: Helicity angle between Z daughter candidates of signal and background events for the $H \to Z\gamma; Z \to q\bar{q}$ channel (a,b), the $H \to Z\gamma; Z \to e^+e^-$ channel (c,d), and the $H \to Z\gamma; Z \to \mu^+\mu^-$ channel (e,f) after pre-selection (a,c,e) and after BDT-selection (b,d,f).

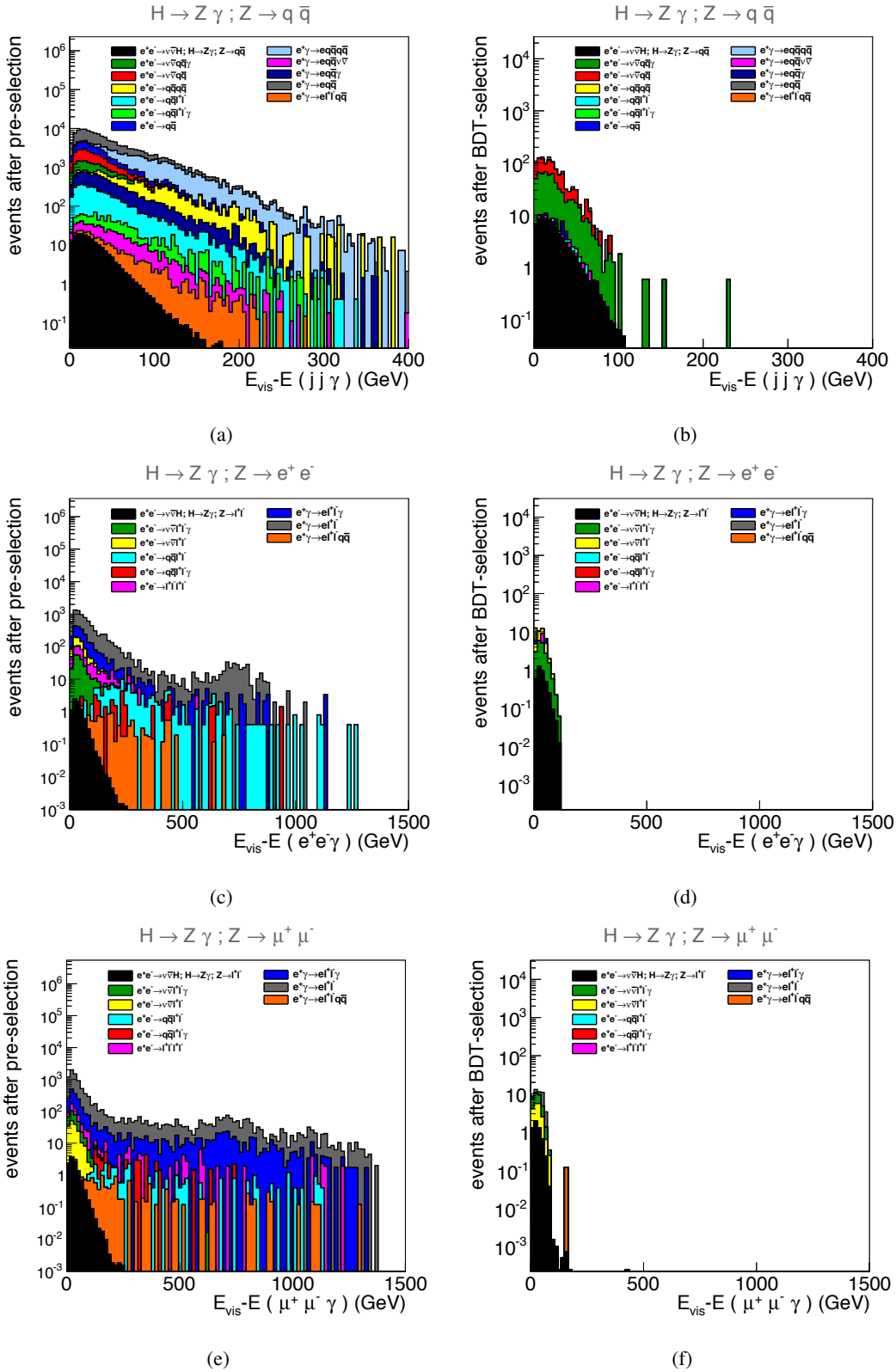

Figure 32: Visible energy without H energy of signal and background events for the $H \to Z\gamma; Z \to q\bar{q}$ channel (a,b), the $H \to Z\gamma; Z \to e^+e^-$ channel (c,d), and the $H \to Z\gamma; Z \to \mu^+\mu^-$ channel (e,f) after pre-selection (a,c,e) and after BDT-selection (b,d,f).

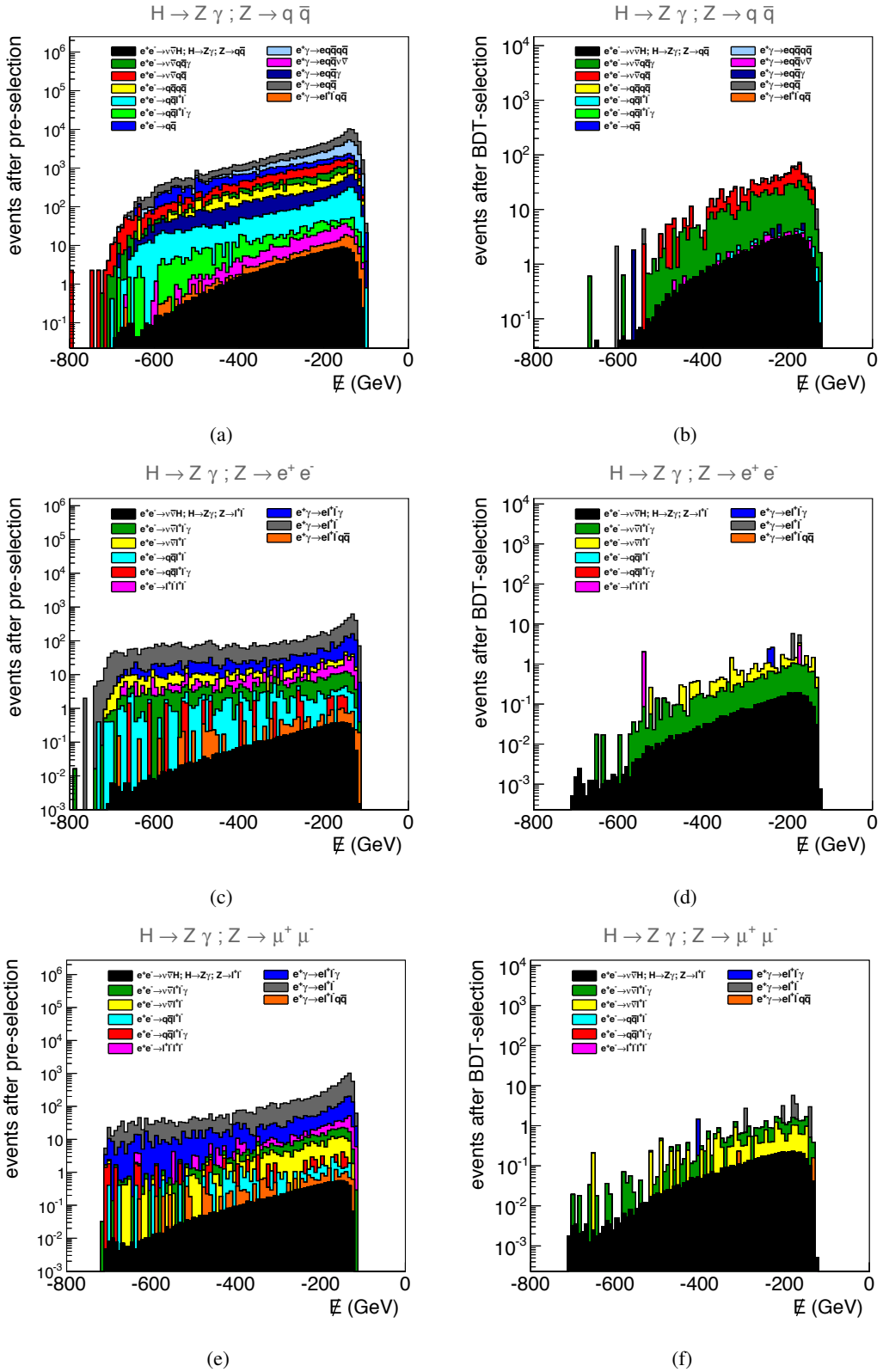

Figure 33: Missing energy in signal and background events for the $H \to Z\gamma; Z \to q\bar{q}$ channel (a,b), the $H \to Z\gamma; Z \to e^+e^-$ channel (c,d), and the $H \to Z\gamma; Z \to \mu^+\mu^-$ channel (e,f) after pre-selection (a,c,e) and after BDT-selection (b,d,f).

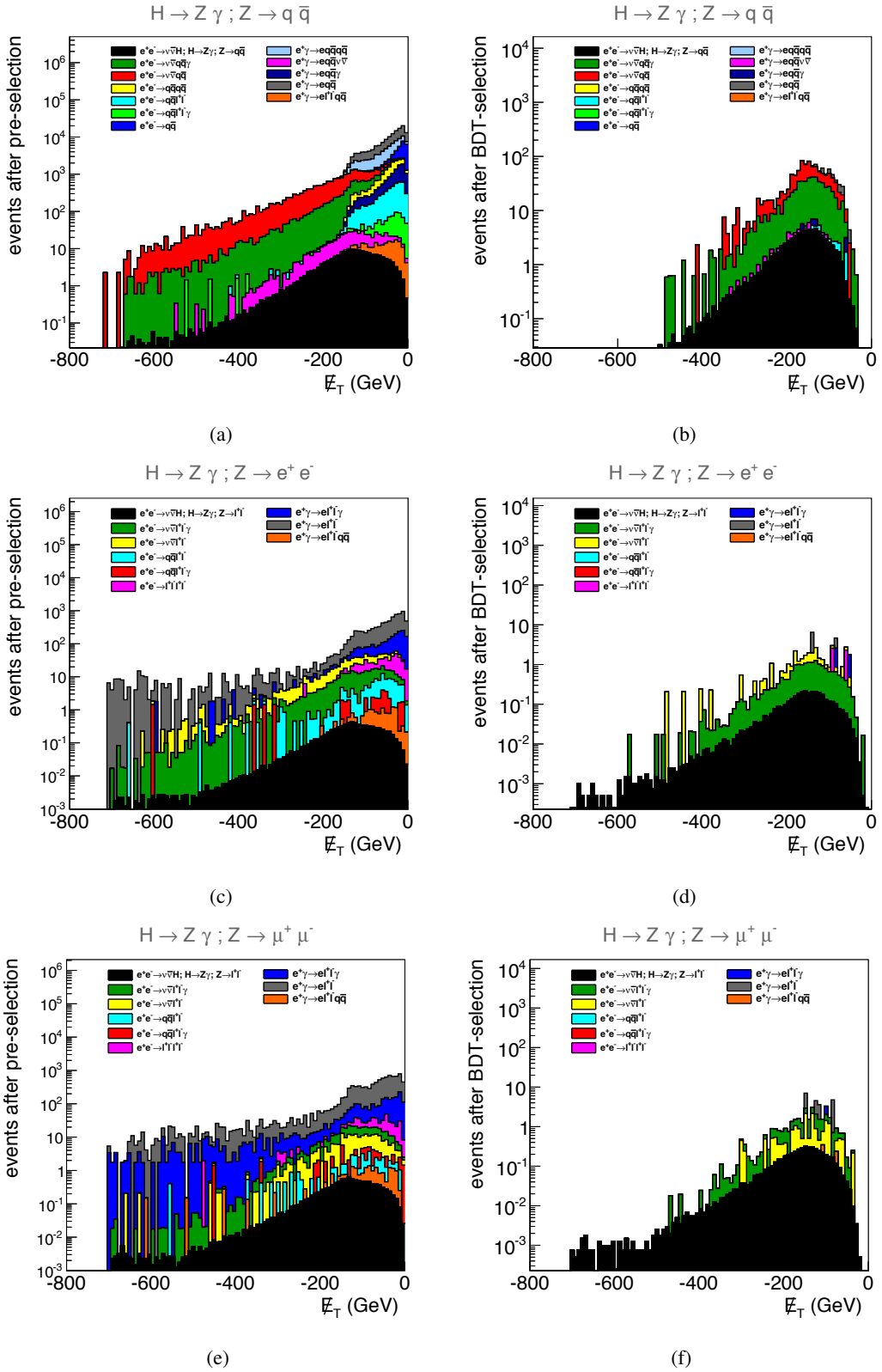

Figure 34: Missing transverse energy in signal and background events for the $H \to Z\gamma; Z \to q\bar{q}$ channel (a,b), the $H \to Z\gamma; Z \to e^+e^-$ channel (c,d), and the $H \to Z\gamma; Z \to \mu^+\mu^-$ channel (e,f) after pre-selection (a,c,e) and after BDT-selection (b,d,f).

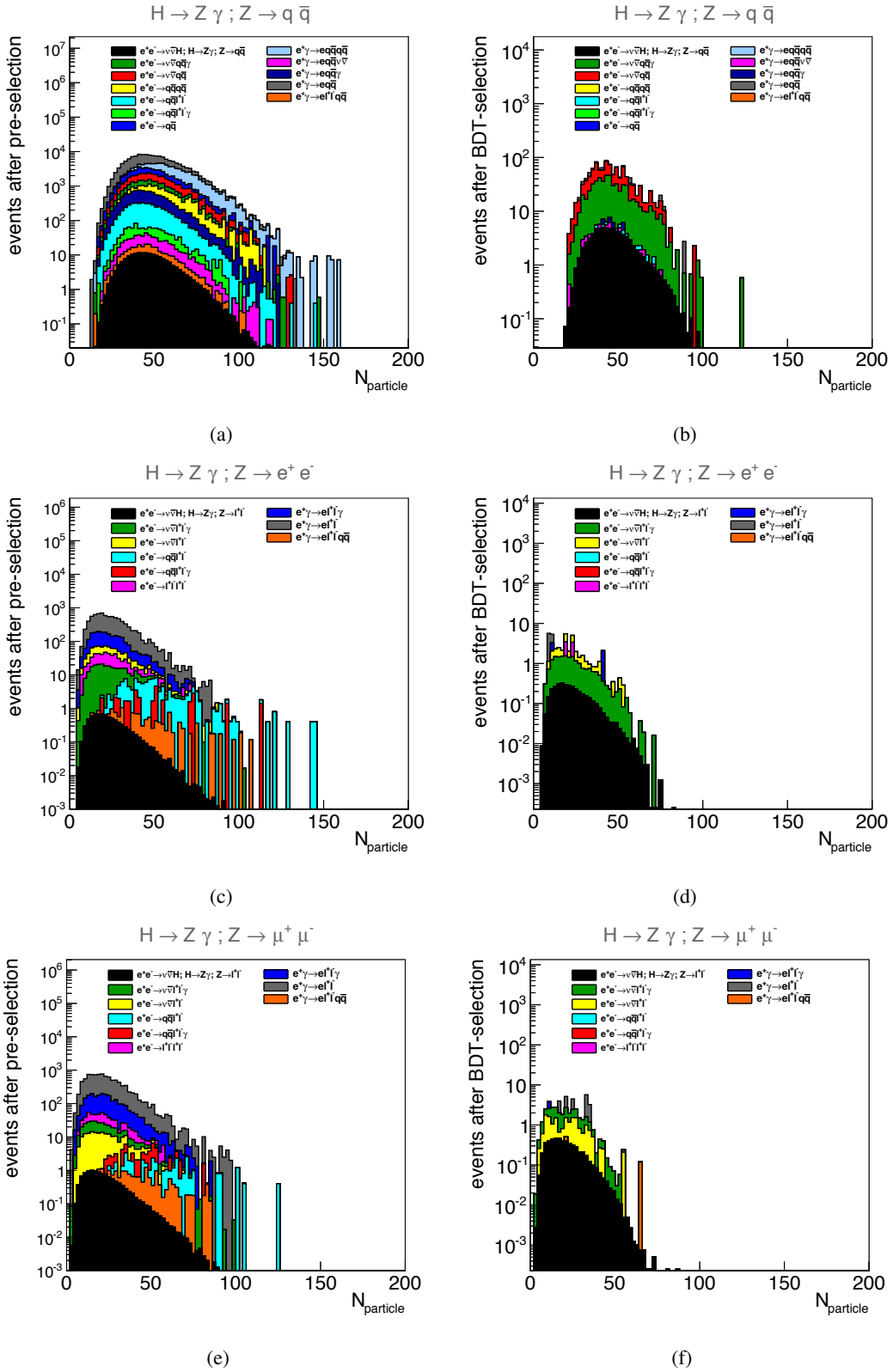

Figure 35: Particle multiplicity ($E > 0\,\text{GeV}$, $p_\text{T} > 0\,\text{GeV}$) in signal and background events for the $\text{H} \to \text{Z}\gamma;\text{Z} \to \text{q}\bar{\text{q}}$ channel (a,b), the $\text{H} \to \text{Z}\gamma;\text{Z} \to \text{e}^+\text{e}^-$ channel (c,d), and the $\text{H} \to \text{Z}\gamma;\text{Z} \to \mu^+\mu^-$ channel (e,f) after pre-selection (a,c,e) and after BDT-selection (b,d,f).

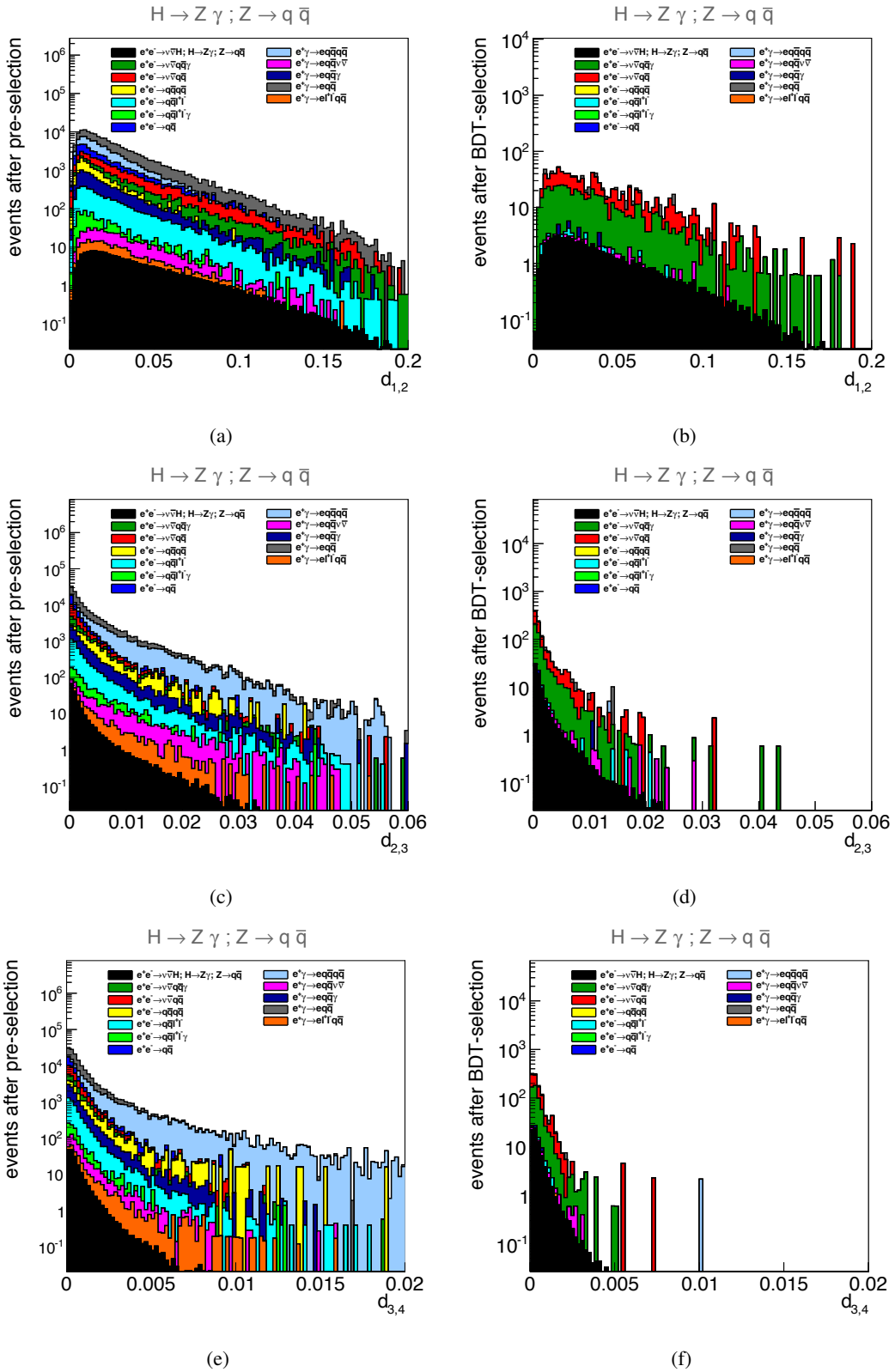

Figure 36: $d_{i,i+1}$ value associated with merging from i to $i+1$ jets in signal and background events for the $H \to Z\gamma; Z \to q\bar{q}$ channel for $i = 1$ (a,b), $i = 2$ (c,d), and $i = 3$ (e,f) after pre-selection (a,c,e) and after BDT-selection (b,d,f).

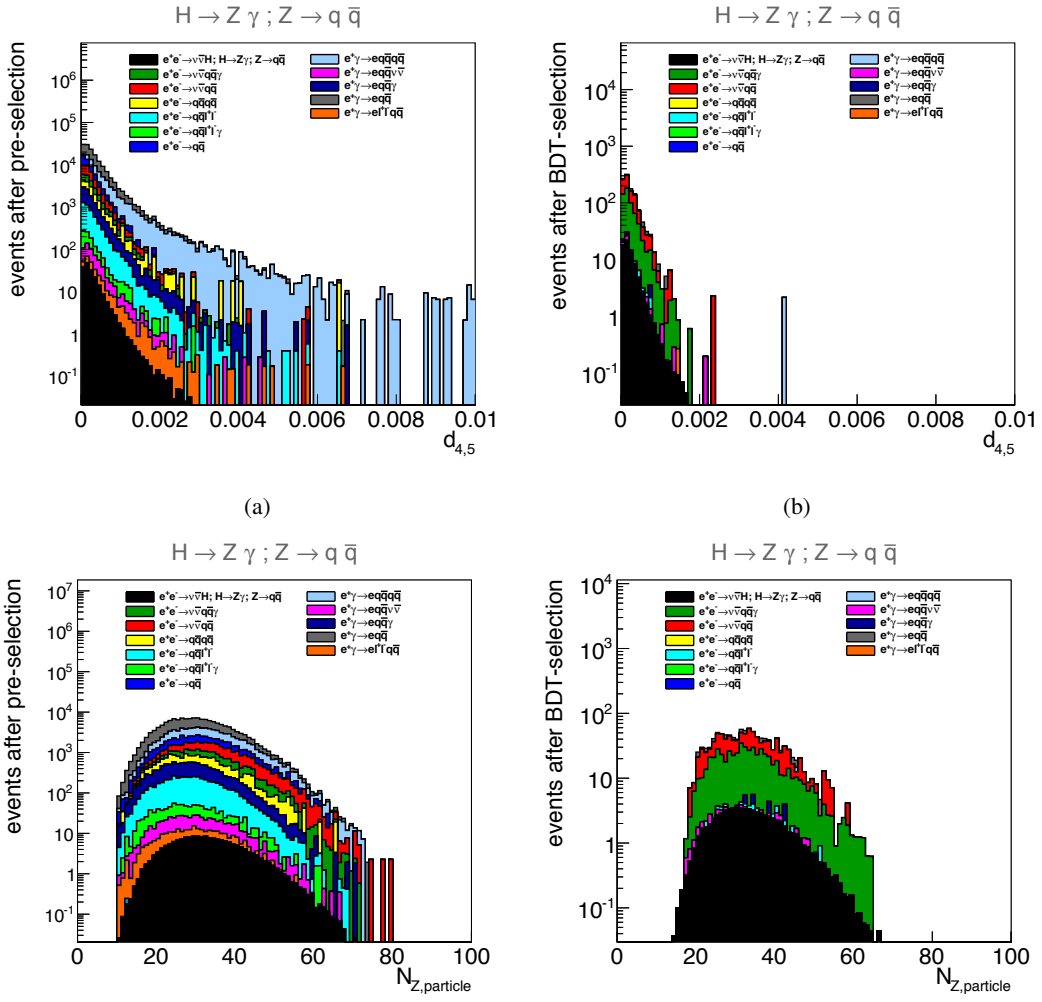

Figure 37: $d_{4,5}$ value associated with merging from 4 to 5 jets (a,b) and particle multiplicity ($E > 0\,\text{GeV}$, $p_\text{T} > 0\,\text{GeV}$) used to reconstruct the Z candidate (c,d) in signal and background events for the $\text{H} \to \text{Z}\gamma;\text{Z} \to \text{q}\bar{\text{q}}$ channel after pre-selection (a,c) and after BDT-selection (b,d).

B. Analysis results from invariant mass fits

In the analysis of a particle decay with a sufficiently large signal to background ratio, the number of signal and background events can be extracted from the invariant mass distribution, using a fit function that describes the expected mass distribution shape. In order not to bias the background "Higgs mass" distribution, the multivariate event selection has to be performed without the particle's invariant mass as an input variable.
In the following, this is tested for the $e^+e^- \to H\nu_e\bar{\nu}_e; H \to Z\gamma$ decay. Figure 38 shows the BDT response distribution for signal and background events as well as the significance, the signal efficiency, and the background efficiency as a function of the BDT selection. Here, the BDT classification of the events is performed without M_H and the M_Z as input variables. It can be seen that for all channels a lower significance is achieved than for the case that M_H and the M_Z are included in the set of input variables of the BDT (cf. Figure 8 and Figure 38).
Due to the extremely low number of signal events, the Higgs mass distributions after BDT selection in Figure 39 do not show clear signal peaks on top of the flat background distribution. Hence, it is not feasable for the $H \to Z\gamma$ channel to extract the number of events using a fit function of the expected shape of the invariant mass distribution.

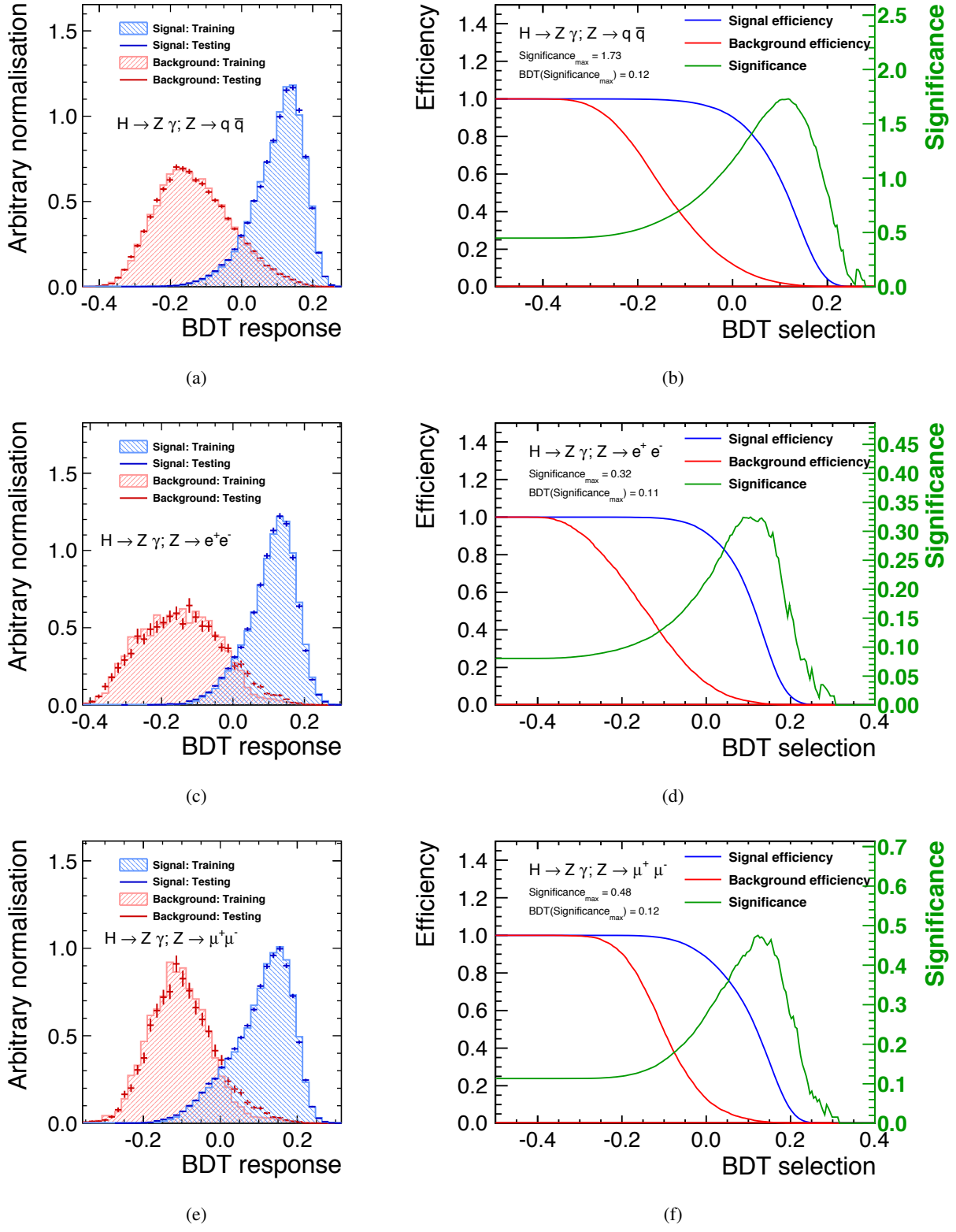

Figure 38: BDT response for signal events (blue) and background events (red) based on kinematic variables introduced in Section 5.2 except for M_{H} and the M_{Z} (a,c,e) and the significance, the signal and the background efficiencies estimated without M_{H} and the M_{Z}, as a function of the BDT selection (b,d,f) for the $\mathrm{H} \to \mathrm{Z}\gamma; \mathrm{Z} \to \mathrm{q}\bar{\mathrm{q}}$ channel (a,b), the $\mathrm{H} \to \mathrm{Z}\gamma; \mathrm{Z} \to \mathrm{e}^{+}\mathrm{e}^{-}$ channel (c,d), and the $\mathrm{H} \to \mathrm{Z}\gamma; \mathrm{Z} \to \mu^{+}\mu^{-}$ channel (e,f). The maximum significance found per channel and the corresponding BDT selection cut are indicated in the figure (b,d,f).

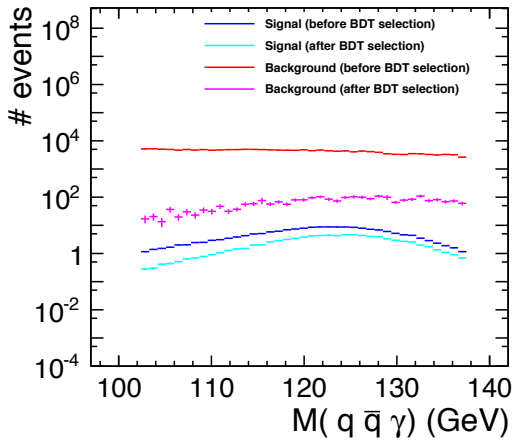

(a)

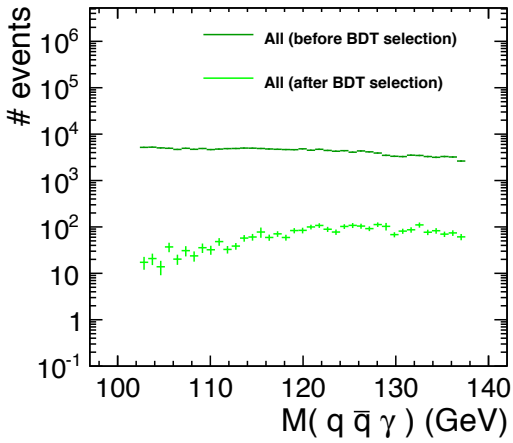

(b)

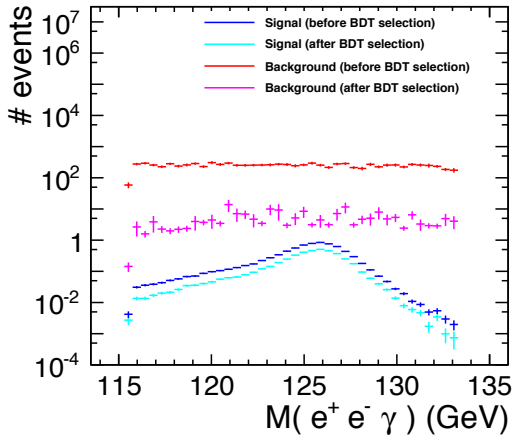

(c)

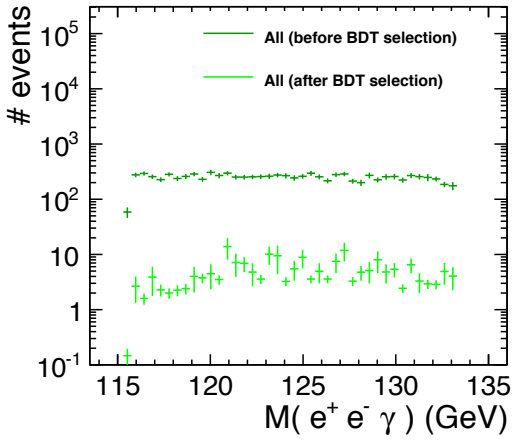

(d)

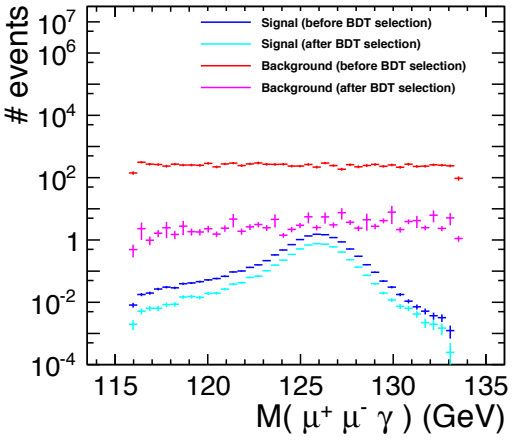

(e)

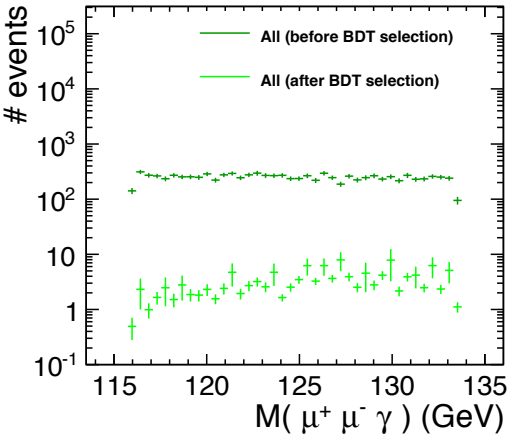

(f)

Figure 39: Reconstructed Higgs mass for signal events (blue, cyan) and background events (red, magenta) before and after BDT selection based on kinematic variables introduced in Section 5.2 except for M_{H} and M_{Z} (a,c,e) and for all events (green) before and after BDT selection (b,d,f), for the $\mathrm{H} \to \mathrm{Z}\gamma; \mathrm{Z} \to \mathrm{q}\bar{\mathrm{q}}$ channel (a,b), the $\mathrm{H} \to \mathrm{Z}\gamma; \mathrm{Z} \to \mathrm{e}^{+}\mathrm{e}^{-}$ channel (c,d), and the $\mathrm{H} \to \mathrm{Z}\gamma; \mathrm{Z} \to \mu^{+}\mu^{-}$ channel (e,f).

References

[1] G. Aad et al., ATLAS Collaboration, *Observation of a new particle in the search for the Standard Model Higgs boson with the ATLAS detector at the LHC*, Phys. Lett. **B 716** (2012) 1, DOI: 10.1016/j.physletb.2012.08.020, arXiv: 1207.7214 [hep-ex].

[2] S. Chatrchyan et al., CMS Collaboration, *Observation of a new boson at a mass of 125 GeV with the CMS experiment at the LHC*, Phys. Lett. **B 716** (2012) 30, DOI: 10.1016/j.physletb.2012.08.021, arXiv: 1207.7235 [hep-ex].

[3] ATLAS Collaboration, *Search for the Standard Model Higgs boson in the* $H \to Z\gamma$ *decay mode with pp collisions at* $\sqrt{s} = 7$ *and 8 TeV*, ATLAS-CONF-2013-009, CERN, 2013.

[4] CMS Collaboration, *Search for the Standard Model Higgs boson in the* Z *boson plus a photon channel in pp collisions at* $\sqrt{s}$ *= 7 and 8 TeV*, CMS-PAS-HIG-13-006, CERN, 2013.

[5] M. Aicheler et al., *A Multi-TeV Linear Collider Based on CLIC Technology* (2012), ed. by M. Aicheler, DOI: 10.5170/CERN-2012-007.

[6] H. Aihara et al., *SiD Letter of Intent* (2009), arXiv: 0911.0006 [physics.ins-det].

[7] C. Grefe, A. Münnich, *The CLIC_SiD_CDR geometry for the CDR Monte Carlo mass production*, LCD-Note-2011-009, CERN, 2011.

[8] L. Linssen et al., eds., *CLIC Conceptual Design Report: Physics and Detectors at CLIC*, CERN-2012-003, CERN, 2012, arXiv: 1202.5940 [physics.ins-det].

[9] P. Lebrun et al., eds., *The CLIC Programme: Towards a Staged* e^+e^- *Linear Collider Exploring the Terascale : CLIC Conceptual Design Report*, 2012, arXiv: 1209.2543 [physics.ins-det].

[10] H. Abramowicz et al., CLIC Detector and Physics Collaboration, *Physics at the CLIC* e^+e^-*- Linear Collider – Input to the Snowmass process 2013* (2013), arXiv: 1307.5288 [hep-ex].

[11] W. Kilian, T. Ohl, J. Reuter, *WHIZARD: Simulating Multi-Particle Processes at LHC and ILC*, Eur. Phys. J. **C 71** (2011) 1742, DOI: 10.1140/epjc/s10052-011-1742-y, arXiv: 0708.4233 [hep-ph].

[12] M. Moretti, T. Ohl, J. Reuter, *O'Mega: An Optimizing matrix element generator* (2001), arXiv: 0102195 [hep-ph].

[13] A. Sailer, *Luminosities for* e^+e^-, $e^\pm\gamma$, *and* $\gamma\gamma$ *interactions*, presentation at the LCD-WG Analysis Meeting http://indico.cern.ch/event/233706/, CERN, May 2013.

[14] T. Sjostrand, S. Mrenna, P. Z. Skands, *PYTHIA 6.4 Physics and Manual*, JHEP **0605** (2006) 026, DOI: 10.1088/1126-6708/2006/05/026, arXiv: 0603175 [hep-ph].

[15] N. Graf, J. McCormick, *Simulator for the linear collider (SLIC): A tool for ILC detector simulations*, AIP Conf. Proc. **867** (2006) 503, DOI: 10.1063/1.2396991.

[16] S. Agostinelli et al., GEANT4, *Geant4: A Simulation toolkit*, Nucl. Instrum. Meth. **A 506** (2003) 250, DOI: 10.1016/S0168-9002(03)01368-8.

[17] J. Allison et al., *Geant4 developments and applications*, IEEE Trans. Nucl. Sci. **53** (2006) 270, DOI: 10.1109/TNS.2006.869826.

[18] *Linear Collider simulations*, URL: http://lcsim.org/software/lcsim/.

[19] M. Thomson, *Particle Flow Calorimetry and the PandoraPFA Algorithm*, Nucl. Instrum. Meth. **A 611** (2009) 25, DOI: 10.1016/j.nima.2009.09.009, arXiv: 0907.3577 [physics.ins-det].

[20] J. Marshall, A. Münnich, M. Thomson, *Performance of Particle Flow Calorimetry at CLIC*, Nucl. Instrum. Meth. **A 700** (2013) 153, DOI: 10.1016/j.nima.2012.10.038, arXiv: 1209.4039 [physics.ins-det].

[21] S. Dittmaier et al., *Handbook of LHC Higgs Cross Sections: 2. Differential Distributions* (2012), arXiv: 1201.3084 [hep-ph].

[22] Particle Data Group, Particle Data Group, *Review of Particle Physics (RPP)*, Phys. Rev. **D 86** (2012) 010001, DOI: 10.1103/PhysRevD.86.010001.

[23] M.-S. Chen, P. M. Zerwas, *Equivalent-Particle Approximations in electron and Photon Processes of Higher Order QED*, Phys. Rev. **D 12** (1975) 187, DOI: 10.1103/PhysRevD.12.187.

[24] H. Abramowicz et al., *A Luminosity Calorimeter for CLIC*, LCD-Note-2009-002, CERN, 2009.

[25] S. Catani et al., *New clustering algorithm for multi-jet cross-sections in* e^+e^- *annihilation*, Phys. Lett. **B 269** (1991) 432, DOI: 10.1016/0370-2693(91)90196-W.

[26] M. Cacciari, G. P. Salam, G. Soyez, *The anti-k_T jet clustering algorithm*, JHEP **04** (2008) 063, DOI: 10.1088/1126-6708/2008/04/063, arXiv: 0802.1189 [hep-ph].

[27] A. Höcker et al., *TMVA - Toolkit for Multivariate Data Analysis*, PoS **ACAT** (2007) 040, arXiv: physics/0703039 [physics].

[28] ATLAS Collaboration, *Projections for measurements of Higgs boson cross sections, branching ratios and coupling parameters with the ATLAS detector at a HL-LHC*, ATL-PHYS-PUB-2013-014, CERN, 2013.

[29] CMS Collaboration, *Projected Performance of an Upgraded CMS Detector at the LHC and HL-LHC: Contribution to the Snowmass Process*, CMS-NOTE-2013-002, CERN, 2013.